Wesleyan University | The Honors College

The Atmospheric Escape of Close-In Gas Giant Exoplanets

by

Kimberly Paragas
Class of 2021

A thesis submitted to the
faculty of Wesleyan University
in partial fulfillment of the requirements for the
Degree of Bachelor of Arts
with Departmental Honors in Astronomy

Middletown, Connecticut | April, 2021

Abstract

Hot Jupiters are exoplanets that are Jupiter-like in mass and size and orbit their host stars in very close proximity. Due to their unique physical properties (i.e., their large radii and small separation from their host stars), they have high transit probabilities establishing them as ideal candidates to study the atmospheric escape of close-in exoplanets. Their short orbital periods expose them to increased irradiation from their host stars, which causes them to lose their atmospheres. The helium (He I) 1083 nm line offers insight into the atmospheric escape of this selection of planets, which is likely to be significant in sculpting their population. By measuring the amount of excess absorption in this line during a transit, we are able to characterize the spatial extent of the planet's exosphere and its corresponding present-day mass loss rate. We used an ultra-narrow band filter to observe two transits of the gas giant HAT-P-18b, using the 200" Hale Telescope at Palomar Observatory, and report the first-ever detection of He I in its atmosphere. We compare our results to *Transiting Exoplanet Survey Satellite (TESS)* data. With a J-band magnitude of 10.8, this is the faintest system for which such a measurement has been made, demonstrating the effectiveness of this approach for surveying mass loss on a diverse sample of close-in gas giant planets. As there has only been a handful of other helium outflow detections, our results directly contribute to the improvement of current atmospheric mass loss models. We used Wesleyan's High Performance Computing Cluster to successfully run `Athena Æ`, a 3D hydrodynamic code that simulates the atmospheric escape of hot Jupiters. We produced a simulation of a generic hot Jupiter to compare to our observational results and built the computational infrastructure at Wesleyan to enable future 3D hydrodynamic modeling of the extended atmospheres of exoplanets.

We cannot change the cards we are dealt, just how we play the hand.

–Randy Pausch

The Last Lecture

Acknowledgements

First and foremost, I am grateful for the support of an Undergraduate Research Grant from the NASA Connecticut Space Grant Consortium that gave me the opportunity to make research my main focus this past year.

I am so thankful for the Astronomy Department for all of their constant support and friendliness throughout my three years here at Wesleyan. There are some people I would like to individually thank for supporting me throughout this endeavor, but I am appreciative of every single person who has been there for me in anyway during this process. I could not thank you all enough.

To Seth: I am incredibly thankful to have had you as my thesis advisor and first astronomy professor. Your passion and enthusiasm for astronomy truly shined during my first astronomy class, ASTR155, and continues to resonate with me as I progress in my academic career. Your constant unwavering support has encouraged me to keep pushing forward countless times and I cannot express how much I have appreciated being able to work with you on this project.

To Heather: Thank you for adopting me into your group this past summer and introducing me to exoplanet research. Your support throughout this past year, from carefully editing my first first author paper to looking over my graduate school applications and everything in between, is something that I will always cherish.

To Shreyas: Thank you for teaching me a plethora of skills and concepts that have been crucial to my ability to do research and my trajectory towards graduate school and beyond. The progress I made on our helium detection was largely made possible by your never-ending patience and availability. Your mentorship throughout this past year has meant so much to me and I hope you know how

grateful I am of all the time you have spent on helping me with research and graduate school applications/decisions.

To Henk: Thank you for your constant communication about Wesleyan's HPCC. Our success in running an entire simulation on the cluster relied on your much appreciated involvement and support. Thank you for being so responsive this past semester and please know that this thesis was made possible because of you.

To Vacek: Thank you for always lending an ear to listen to me talk about my thesis troubles. I always looked forward to being able to update you on my progress every week and I will miss you very much next year.

To Fallon: Thank you for being my dedicated work buddy throughout the past year. Somehow the pandemic brought us even closer than we were when we saw each other every day in the basement of VVO. I am so thankful to be able to call you my friend. Thank you for always being there to chat about absolutely anything. I look forward to seeing you excel in your graduate career and to our future trips (.i.e., our road trip and rogue takes on Japan)!

To my family: Tom, thank you for always listening to me talk about my research over and over again. Your partnership has gotten me through the roughest patches and I cannot thank you enough for always being there for me. Kuya Chris, thank you for never failing to make me laugh, and reminding me not to take everything so seriously. Mom, thank you for pushing me to be the best that I can be everyday. I hope that I am making you proud. I am thankful to all of you for your constant support throughout every endeavor I pursue. I love you all so much.

Contents

1 Introduction **1**

1.1 Exoplanets 1

1.2 Transits 3

1.3 Atmospheric Mass Loss 6

1.3.1 Methods of Detection 9

1.3.2 Helium as a Probe 10

1.4 Atmospheric Mass Loss Models 11

1.5 HAT-P-18b 14

1.6 A Closer Look at Extended Exoplanetary Atmospheres 15

2 Observations & Data Reduction **17**

2.1 WIRC Observations 18

2.2 *TESS* Observations 25

3 Light Curve Modeling and Fitting **27**

3.1 Modeling with `exoplanet` 27

3.2 Fitting with `PyMC3` 28

4 Helium Results & Discussion **36**

4.1 Excess Helium Absorption for HAT-P-18b 36

4.2 Constrained Atmospheric Escape Rate for HAT-P-18b 37

4.3 Hot Giant Planets Orbiting K-Type Stars 43

4.4 HAT-P-18b Direct Comparison to WASP-107b 44

5 Atmosphere Modeling **47**

5.1 Introduction to `Athena Æ` 47

5.2 Parameters 48

5.3 Test Run 50

5.3.1 Set-Up 50

5.3.2 Running `Athena Æ` on Wesleyan's High Performance Computing Cluster (HPCC) 50

5.4 Small Simulation Preliminary Results 55

6 Conclusion **64**

6.1 Future Work 64

6.1.1 Future Helium Targets 64

6.1.2 The Effect of Planetary Magnetic Fields on Outflows . . . 65

6.1.3 Modeling HAT-P-18b 66

Bibliography **68**

Chapter 1

Introduction

1.1 Exoplanets

It has been nearly three decades since the very first detection of a planet orbiting a star outside of our solar system. Wolszczan & Frail (1992) used pulsar timing variations to identify a system of two or more planets orbiting the pulsar PSR1257+12. This first detection introduced the possibility of a new, exciting field in astronomy: exoplanets. A few years later, in 1995, the first exoplanet found to be orbiting around a solar-type star was discovered via the radial velocity (RV) technique (Mayor & Queloz 1995), which takes advantage of the Doppler shift, a method that was developed to study stars through observing the shift in wavelength caused by the motion of a star along our line of sight. But, if there exists a massive and close enough planet to its host star, its gravitational influence can cause its host star to wiggle, resulting in a small observable Doppler shift (Struve 1952). This planet, 51 Pegasi b, is estimated to have a semi-major axis of 0.052 AU, an orbital period of $\sim$4 days, and a mass of 0.5 Jupiter masses ($M_{\rm J}$) (Martins et al. 2015). This detection was particularly shocking because we lack a close-in, giant planet in our own solar system, which raised skepticism among the astronomy community (Walker 1995). But, 51 Pegasi b was the first of many planets of its kind to be detected, now known as "hot Jupiters," which are

defined as planets that are similar in size and/or mass to Jupiter and orbit in very close proximity to their host star. Today, we have detected over 4000 exoplanets and about 350 planets are hot Jupiters [1]. This population of planets are shown in red in Figure 1.1. In addition, close-in gas giants are interesting targets to study to answer the many open questions within the field. How did these planets become so close to their host star? What are these planets made of? What is their origin? What is their fate? Not only have we come a long way from merely detecting exoplanets, we are now able to gain a deeper understanding of the many exoplanets throughout our galactic neighborhood.

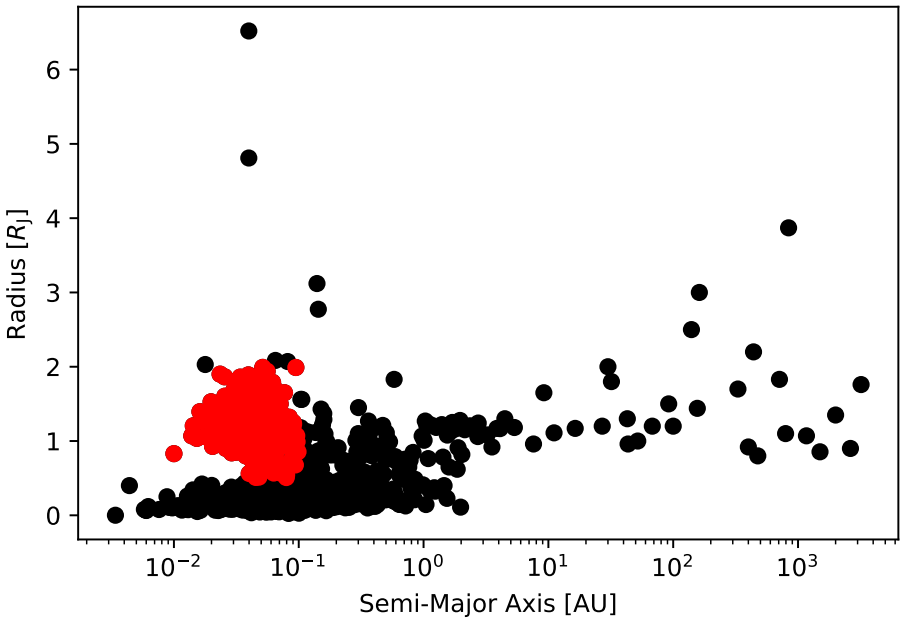

Figure 1.1: The radius as a function of semi-major axis of all discovered exoplanets (data from The Extrasolar Planets Encyclopedia) with the red points being planets that have radii between $0.5R_J$ and $2R_J$, where R_J is the radius of Jupiter, with a separation less than 0.1 AU.

[1] https://exoplanetarchive.ipac.caltech.edu/

1.2 Transits

Thousands of exoplanets have been discovered throughout the last three decades and we continue to be able to characterize them in more detail. The two major telescopes that have contributed to the study of exoplanets are *Kepler* and the *Transiting Exoplanet Survey Satellite (TESS*). The *Kepler* space telescope was launched into orbit by NASA in 2009 and retired in 2018. During its nine year mission, *Kepler* detected 2662 exoplanets, which is more than half of the currently known exoplanet population. In the same year Kepler retired, NASA launched *TESS* which is able to observe an area that is 400 times larger than *Kepler* (Ricker et al. 2014), and is still in commission in an extended mission as of April 2021. Both of these telescopes were designed to detect exoplanets using the transit method, a primary mechanism through which exoplanets are discovered and characterized.

According to the NASA Exoplanet Archive [2], 76% of discovered exoplanets were detected using the transit technique, which is illustrated in Figure 1.2. The huge spikes in exoplanet discoveries between 2013 and 2018 were made possible by the *Kepler* mission, alongside major ground-based searches. A transit occurs when an exoplanet travels between its host star and the observer, therefore, a percentage of the observed starlight is blocked by the planet. By quantifying the amount of starlight that is blocked, typically between 0.01% and 1% (Winn 2010), we can create light curves that contain information about the planet's structure, orbital characteristics, and composition. The percentage of the light blocked encodes information about the planet's size, while the duration of the transit encodes information about its orbital inclination and distance to its host

[2]https://exoplanetarchive.ipac.caltech.edu/

star. We can estimate the planets radius using

$$\delta = \left(\frac{R_{\rm p}}{R_\star}\right)^2,$$

where δ is the transit depth, or the percentage of light blocked during the mid-transit time, $R_{\rm p}$ is the radius of the planet, and $R_\star$ is the radius of the star. The amount of starlight blocked by a planet is only on the order of a percent because stars are much larger than their planets. For example, if we were to observe Jupiter transiting our Sun, we would measure a transit depth of about 1%, while the transit depth of Earth would be about 0.08%. Notice that the largest planets, such as hot Jupiters, and the smallest stars, such as K and M stars, produce the largest signals, making them the most ideal targets for this method. Figure 1.3 demonstrates a transiting exoplanet and its corresponding light curve.

Being able to observe a transit is an occurrence that requires many aspects to be in the observer's favor. The planet's orbit must be edge-on, or at least very close to it, as a face-on system would not allow for an observer to detect a planet occulting its host star. This requirement alone excludes many systems from being detected using this method. In general, the probability of a transit to occur when marginalizing over all possible arguments of periapse ω values is given by

$$\mathrm{p_{tra}} = \left(\frac{R_* \pm R_p}{a}\right)\left(\frac{1}{1-e^2}\right),$$

where R_* and $R_{\rm p}$ are stellar and planet radius, respectively, a is the semi-major axis, and e is the eccentricity (Winn 2014). From this equation, we can see that the probability is indirectly proportional to the semi-major axis a, which means planets with small separations from their host stars have higher transit probabil-

ities. Additionally, planets with larger radii will block more of the starlight we receive, thus, close-in gas giants, the hot Jupiters, are optimal targets for this technique.

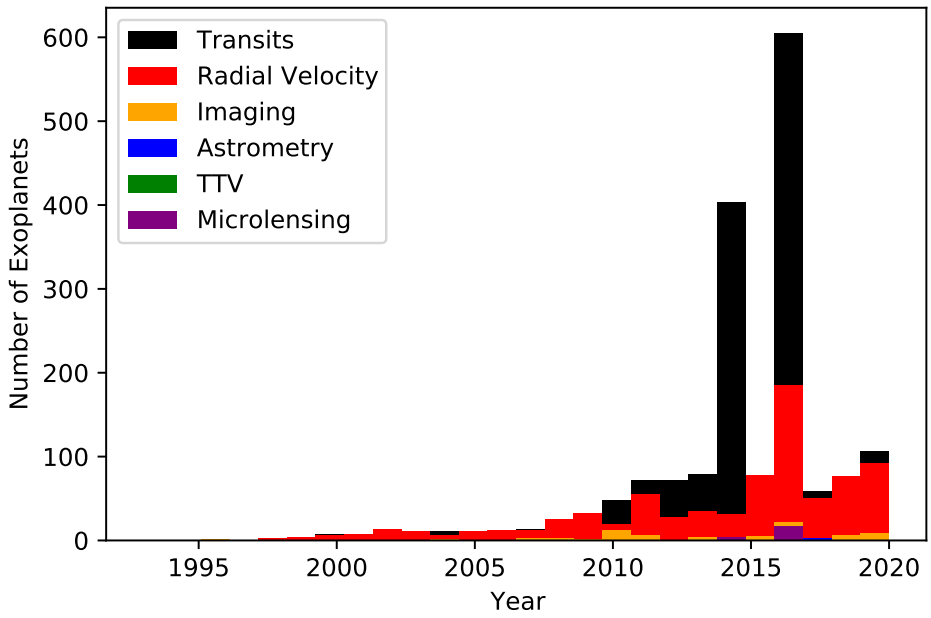

Figure 1.2: The distribution of exoplanets discovered via the transit method (in black), radial velocity (in red), imaging (in orange), astrometry (in blue), transit timing variations (in green), and microlensing (in purple). Notice the transit method dominates over all other techniques. Source of the data: The Extrasolar Planets Encyclopedia

The transit method can further be used to characterize atmospheres of exoplanets. Some of the starlight that we observe during a transit will interact with the upper atmosphere of the exoplanet, and at particular wavelengths, the upper atmosphere will appear opaque, thus increasing the effective transit depth. So, this extra absorption of starlight will make the planet appear larger to the observer. For example, the Earth's atmosphere is transparent in visible wavelengths, but opaque in the UV and X-ray wavelengths. Additionally, interactions between

the host star and its planet may cause atmospheric mass loss within the planet which can be tracked via the transit depth as well. For example, the stellar wind particles of a planet's host star can heat the planet's atmosphere causing molecules to escape the planet's gravitational pull. Thus, the transit method tracks not only the size of the planet itself, but also its atmosphere and any trailing gases from atmospheric escape.

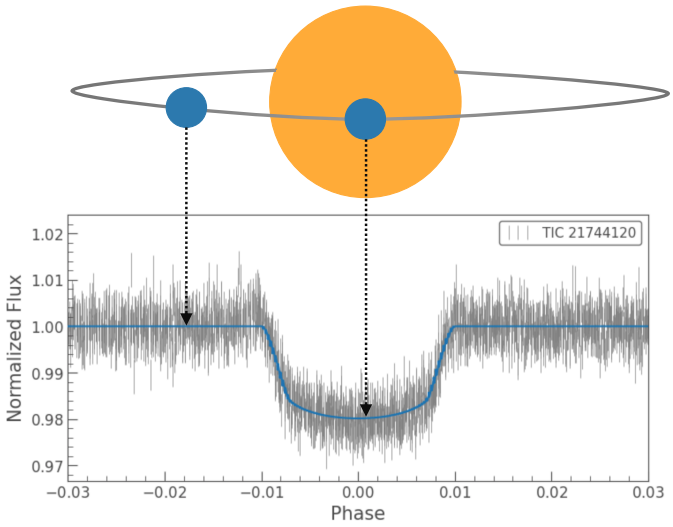

Figure 1.3: Our target, HAT-P-18b (see Section 1.5 for more details), shown transiting with its physical positions before and during transit and its corresponding positions on the light curve.

1.3 Atmospheric Mass Loss

The proximity of close-in exoplanets to their host stars can lead to interactions that may cause atmospheric mass loss from the planet. High-energy stellar radiation shapes the observed exoplanet population via atmospheric escape (e.g., Fulton et al. 2017), so observations of mass loss can directly probe exoplanet

evolution. The literature indicates that it may be possible for a planet to lose such a significant portion of their atmospheric mass that it could convert from a Neptune-sized planet to a super Earth, a planet that is slightly larger in size and/or radius than Earth. The most massive planets, the Jupiters, are massive enough to hold onto their atmospheres, while the lower mass, terrestrial planets are unable to retain any hydrogen or helium in their atmosphere. But, planets that are smaller than Neptune lie at a fork in the exoplanet evolutionary track where they may be able to hold onto their H/He atmospheres, or lose them and turn into lower mass planets more comparable to super Earths. This evolutionary crossroads may be the driving force of the "Fulton Gap," named after Benjamin Fulton who has done substantial work on the distribution of the exoplanet population. This gap refers to the observed shortage of exoplanets with radii between $1.5R_{\oplus}$ and $2R_{\oplus}$, where $R_{\oplus}$ is the radius of the Earth (Fulton et al. 2017). Continuing to study atmospheric mass loss in exoplanets can give us insight into how the observed population of extrasolar planets known to date reached their current state.

Additionally, atmospheric escape is known to have sculpted our own solar system's innermost planets (Tian et al. 2013; Tian 2015). In particular, the escape of the oceans of Venus was likely due to the effects of hydrodynamic winds from our Sun, which deemed it insuitable to harbor life. Additionally, studies enabled by the Mars Atmosphere and Volatile Evolution (MAVEN) spacecraft have found that a significant amount of Mars' atmospheric mass has been lost, which played a role in forming the planet's currently cold and dry atmosphere (Jakosky et al. 2017). Thus, understanding atmospheric mass loss is necessary to uncover the evolutionary process of the general exoplanetary population, and to reveal the evolution of atmospheres in our own solar system.

A planet that is experiencing mass loss will have an atmosphere that extends past its Roche lobe, the area where material is gravitationally bound to the planet. A planet's Roche lobe radius $R_{\rm Roche}$ is given by

$$\left(\frac{R_{\rm Roche}}{R_\star}\right)^2 \approx 0.13 \left(\frac{a}{0.025\ {\rm AU}}\right)^2 \left(\frac{M_p}{M_J}\right)^{2/3} \left(\frac{R_\star}{R_\odot}\right)^{-2} \left(\frac{M_\star}{M_\odot}\right),$$

where $R_\star$ is the radius of the host star, a is the semi-major axis of the planet, M_p is the mass of the planet, M_J is the mass of Jupiter, $R_\star$ is the radius of the host star, $R_\odot$ is the radius of the Sun, $M_\star$ is the mass of the star, and $M_\odot$ is the mass of the Sun (Owen 2019). For reference, the Earth's Roche radius is about 1.5×10^6 km, while the Roche radius of a typical hot Jupiter orbiting a solar-type star is about 5.6×10^5 km.

Atmospheric escape can occur through both non-thermal (e.g., charge exchange, magnetic field lines to the star, or photochemical reactions) and thermal processes, but in this work, we focus on close-in planets, which are exposed to extreme radiation from their host stars, so thermal escape is far more influential than non-thermal escape. Two thermal processes known to cause atmospheric mass loss are Jean's escape and hydrodynamic escape (Tian 2015). Jean's escape occurs when the atmospheric molecules in the high-end tail of the Maxwell velocity distribution, where they have higher speeds than the average molecule, may reach escape velocity, thus leaving the atmosphere, while hydrodynamic escape occurs when molecules in a planet's atmosphere are heated from the Extreme Ultra-Violet (EUV) radiation of its host star and are pushed out and above the escape velocity. Thus, hydrodynamic escape is much more significant than Jean's escape. So, in this work, we focus on the latter thermal process, hydrodynamic escape.

1.3.1 Methods of Detection

There are many methods for detecting mass loss: absorption in the hydrogen (H) Lyman-α (Lyα) line, absorption in the Hα line, the detection of metals in the UV and optical, and absorption in the helium (He I) 1083 nm transition line.

Prior to 2018, most studies of atmospheric escape have been at UV wavelengths using the Lyman-α line at 121.6 nm. It is the spectral line of hydrogen emitted when its electron falls from the $n = 2$ to the $n = 1$ orbital. It was detected for the first time in the atmosphere of HD 209458b using the *Hubble Space Telescope (HST)* (Vidal-Madjar et al. 2003). Although detections using this method have been fruitful in constraining the mechanisms of mass loss, this method has many limitations. At the moment, Lyα detections are only possible using *HST*, making it challenging to observe regularly. Once the *HST* mission is complete, Lyα measurements will come to a halt, as the *James Webb Space Telescope (JWST)* will not be able to make observations in this line. Moreover, the Lyα line is heavily affected by interstellar medium absorption and geocoronal emission, making it difficult to obtain mass loss measurements.

An alternative method is to use the absorption in the Hα line. Hα is a deep-red, visible spectral line in the Balmer series with a wavelength of 656.3 nm. It occurs when a hydrogen electron falls from its third to second lowest energy level. This method was first used to detect atmospheric escape in the atmosphere of HD 189733b (Jensen et al. 2012). If one can detect both Lyα and Hα in the atmosphere of an exoplanet, one can constrain the excitation temperature of the exosphere. Although exciting, detections in this line are difficult as it can be heavily influenced by the host star's stellar activity (Cauley et al. 2018).

Atmospheric mass loss has been detected using the presence of metals in the

UV and the optical. Oxygen and carbon were detected in the atmosphere of HD 209458b in the UV, indicating the presence of metals up to and beyond the Roche lobe of the planet (Vidal-Madjar et al. 2004). The neutral magnesium triplet (Mg I) has been shown to be able to estimate a planet's mass loss rate depending on the brightness of the host star and the escape rate of magnesium (Bourrier et al. 2015). Additinally, Mg I has been detected in the optical of the hot Jupiter KELT-9b (Cauley et al. 2019), establishing magnesium as a probe of atmospheric escape.

1.3.2 Helium as a Probe

Within the last couple of years, a new method for detecting atmospheric mass loss has emerged. The helium triplet (He I) feature at 1083 nm was first introduced to be useful for atmospheric mass loss studies in 2000 (Seager & Sasselov 2000). In this line, a planet's low-density upper atmosphere becomes opaque, revealing outflowing material though an increased transit depth (Oklopčić & Hirata 2018). The amount of He I in a planet's atmosphere is strongly dependent on the hardness of its host star's spectra, i.e., the ratio of its flux intensity at mid-UV to extreme-UV wavelengths, making K-type stars the most favorable targets (Oklopčić 2019). While K-type stars are optimal, it is still possible for planets orbiting G- or M-type stars to have a sufficient population of metastable helium atoms enabling an extended (potentially escaping) helium atmosphere detection. The first detection using this line came 18 years after Seager & Sasselov (2000) suggested its potential when He I absorption was measured in the atmosphere of WASP-107b (Spake et al. 2018) using the Wide-Field Camera 3 (WFC3) on *HST*. This line is a more observationally accessible alternative to the Lyα line, as it is

observable using ground based facilities. There have been 5 other unique helium detections in the atmospheres of HD 189733b, HD 209458b, HAT-P-11b, WASP-69b, and GJ 3470b using both space and ground based facilities (Allart et al. 2018; Mansfield et al. 2018; Nortmann et al. 2018; Salz et al. 2018; Alonso-Floriano et al. 2019; Ninan et al. 2020). Of these six planets, four orbit K-type stars, while the remaining two orbit G- and M-type stars. An example of a novel ground-based approach is presented in Vissapragada et al. (2020), where they detect He I using an ultra-narrow band filter centered on the 1083 nm line installed on the 200" Hale Telescope at Palomar Observatory. Further, they constrain a mass loss rate for WASP-69b and place an upper limit on excess helium absorption for WASP-52b. Together, Lyα, Hα, and He I observations can further constrain mass loss models as they probe different parts of a planet's atmosphere (Oklopčić & Hirata 2018). Through studying these mass loss rates, one can gain insight into the relationship between a planet and its host star.

In this thesis, we will present an atmospheric mass loss interpretation of the extended atmosphere of the gas giant HAT-P-18b with a narrow band filter approach similar to Vissapragada et al. (2020). As there are only 6 unique helium outflow detections to-date, this detection is important for further constraining current theoretical atmospheric mass loss models.

1.4 Atmospheric Mass Loss Models

There are a plethora of theoretical atmospheric mass loss models developed by various groups to analyze the dynamics of mass loss for exoplanets experiencing increased radiation from their host stars (e.g., Yelle 2004; Murray-Clay et al. 2009; Owen & Jackson 2012; Oklopčić & Hirata 2018; McCann et al. 2019).

Most models thus far have been one dimensional, with a few multi-dimensional approaches. Even within the 1D models, they still differ in their initial assumptions. For example, they have different assumptions in the percentage of energy being converted to heat and/or the H/He fraction, and even differing methods of calculation. Due to these differences, they conclude varying relationships between mass loss rate and input energy flux. Although these models differ, and thus, have different predictions, an increase in observations of atmospheric mass loss directly translates to the improvement of the constraints on the dynamics of atmospheric escape. Here we discuss a one dimensional and a three dimensional model.

We first introduce a simple 1D hydrodynamic atmospheric escape model detailed in Oklopčić & Hirata (2018). Their model is founded upon the assumption that the upper escaping atmosphere of a planet can be well described by an isothermal Parker wind, which is the expanding stellar corona that produces a stellar wind comprised of a stream of particles driven by gas pressure (Parker 1958). For additional simplicity, they assume that the outflow is spherically symmetric. The model has four free parameters: planetary mass, planetary radius, wind temperature, and mass loss rate. First, they compute 1D density and velocity profiles for a hydrogen-helium atmosphere described by an isothermal Parker wind that spans a specific wind temperature range and mass loss rate range. The model is unable to predict these values, so they must be assumed. Next, they calculate level populations of hydrogen and helium for each profile. These profiles can then be translated into a transit depth estimation in the He I 1083 nm line. Due to its simplicity, the model is less detailed than 3D models, so it is unable to identify differences in the wind properties of the dayside and nightside of the planet or a cometary tail of material trailing from the planet. Additionally, it does not model the interaction between escaping material and the stellar wind. Fortunately, it

is computationally inexpensive, which allows for a broader range of exploration with a variety of parameters.

Alternatively, the 3D radiative hydrodynamic simulations of atmospheric escape using `Athena Æ` described in detail in McCann et al. (2019) is able to model the hydrogen atmospheres of tidally locked planets that are receiving large amounts of ionizing extreme-ultraviolet flux in various stellar regimes. Specifically, `Athena Æ` can model asymmetrical processes that can reveal information about the interaction between a planet's escaping material and the stellar wind of its host star. They take a bottom-up approach where they apply aspects of a stellar environment, namely, the ionizing flux, the tidal potential, and the stellar wind, individually to predict how each produces observable properties. The model is able to predict the density structure of an escaping atmosphere and the temperature of the escaping gas for various stellar regimes. There are three classes of simulations: Rogue, Tidal, and Rotating. The Rogue class is the base case with a planet experiencing ionizing flux without a stellar wind. The Tidal class includes tidal forces, in addition to the ionizing flux. The Rotating class is the Tidal class with the Coriolis force added. The density profiles for varying stellar wind strengths in a full Rotating frame are shown in Fig 1.4. In the weakest stellar wind regime, the planetary outflow is able to extend freely towards the bounds of the simulation, while in the strongest stellar wind regime, the planetary gas is completely enclosed by the stellar wind, forming a cometary structure. Due its complexity, this model is much more computationally expensive, resulting in run times on the order of 10 or more days. In this work, we plan to utilize the 3D simulations of `Athena Æ` to model the atmosphere of a generic hot Jupiter and comprehend it in the context of our target, a close-in gas giant exoplanet.

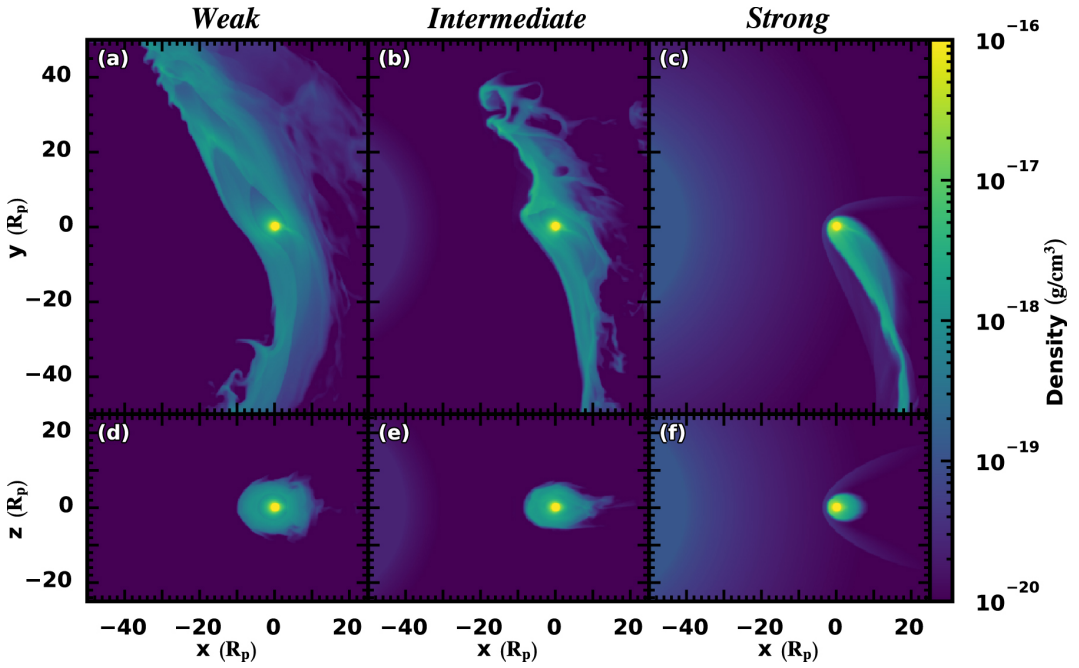

Figure 1.4: A still of the density structure of a hydrodynamic, escaping planetary hydrogen gas outflow with varying stellar wind strengths in a full Rotating frame. The top row is a view from the orbital plane and the bottom row is a view from the planet-star axis. This is Figure 10 in McCann et al. (2019).

1.5 HAT-P-18b

Our target, HAT-P-18b, is named after the Hungarian-made Automated Telescope (HAT) [3] surveys that began in 2003 and aimed to search for exoplanets using small robotic telescopes. HAT-P-18b (Hartman et al. 2011), is a Jupiter-like in size ($0.947 \pm 0.044 R_J$) and Saturn-like in mass ($0.196 \pm 0.008 M_J$) planet with an equilibrium temperature of 841±15 K (Esposito et al. 2014), that orbits a K2-type star with $J = 10.8$ (Cutri et al. 2003). Its Rossiter-McLaughlin effect was measured using the High Accuracy Radial velocity Planet Searcher - North (HARPS-N) spectograph on the 3.58 meter Galileo National Telescope (TNG) located in La Palma in the Canary Islands, Spain, which determined that the

[3] https://hatsurveys.org

planet orbits in retrograde, making it one of the only planets around a cool main sequence star to have a counter-rotating orbit (Esposito et al. 2014). In 2015, ground based observations of multiple transits of HAT-P-18b were made to search for transit timing variations (TTVs), but they found no significant evidence to confirm a TTV for this system (Seeliger et al. 2015). Additionally, the planet is speculated to have a high-altitude haze due to its detected Rayleigh blueward scattering slope determined from ground based transmission spectroscopy (Kirk et al. 2017). Most recently, a secondary eclipse of HAT-P-18b was detected and used to estimate a brightness temperature of 1004^{+78}_{-94} K and 783^{+77}_{-100} K in the 3.6μm and 4.5μm bands, respectively, for the planet (Wallack et al. 2019). These temperatures were consistent with its equilibrium temperature, suggesting that the planet may have efficient day-night circulation and/or a nonzero albedo. Our work is the first to characterize the extended atmosphere of HAT-P-18b via helium outflow.

1.6 A Closer Look at Extended Exoplanetary Atmospheres

In this thesis, we present the first-ever detection of outflowing gas from the atmosphere of HAT-P-18b. This is only the seventh exoplanet with detected helium absorption, and the faintest system for which such a measurement has been made thus far. We then fit this signal with a 1D atmospheric mass loss model by Oklopčić & Hirata (2018) to estimate its present-day mass loss rate. Lastly, we model the escaping atmosphere of a generic close-in gas giant using `Athena Æ` by McCann et al. (2019) and relate it to our target, HAT-P-18b. We

conclude with a discussion on potential future work relating to atmospheric mass loss for the population of close-in planets and what it means for their long-term evolution.

Chapter 2

Observations & Data Reduction

We observed two transits of HAT-P-18b with the 200" Hale Telescope at Palomar Observatory located in San Diego County, California using an ultra-narrow band filter centered on the helium transition line with the Wide-field InfraRed Camera (WIRC; Wilson et al. 2003). Additionally, we use *TESS* data taken from two different sectors starting on May 14 2020 and June 9 2020 to determine an optical transit depth of HAT-P-18b as a comparison for our helium measurement. We report the first-ever detection of outflowing gas from its upper atmosphere at a confidence level of 3.9σ.

Most metastable helium measurements thus far have used spectrometers installed on both ground- and space-based facilities, making our ground-based ultra-narrow band photometry approach quite different to previous studies. A consequence of our approach is that we do not measure the He I line shape, thus our detection allows us to confidently identify an extended helium atmosphere for the planet, but requires complementary spectroscopic measurements to determine if the planet indeed has an escaping atmosphere. Our ultra-narrow band filter approach is best used in tandem with a spectrometer in order to more closely study a system. Although this narrow band filter installed on the 200" Hale Telescope is the first of its kind for helium studies, previously, narrow band filters have been used for transmission spectroscopy on other facilities for other lines, i.e., the Op-

tical System for Imaging and low Resolution Integrated Spectroscopy (OSIRIS) installed on the 10.4 m Gran Telescopio Canarias (GTC) that can observe at two narrow bandpasses, 790.2 nm and 794.3±2 nm (Colón & Ford 2011).

2.1 WIRC Observations

We observed two transits of HAT-P-18b on UT June 6 2020 (hereafter night 1) and July 8 2020 (night 2) using an ultra-narrow band filter centered on the helium 1083 nm line with a full width at half maximum (FWHM) of 0.635 nm (Vissapragada et al. 2020). Typically when observing, we utilize a custom beam-shaping diffuser that creates a 3" diameter top hat Point Spread Function (PSF; Stefansson et al. 2017), which reduces time-correlated systematics, such as non-uniform pixel response, atmospheric seeing effects, or imperfect guiding, through increasing observing efficiency and minimizing PSF variations. However, due to poor weather conditions on night 1, we instead defocused the telescope to $1\farcs2$, as the use of the diffuser would have introduced additional sky background, thus affecting the precision of our photometry. Night 2 had significantly better weather conditions, so we used the beam-shaping diffuser as usual.

Our narrow bandpass causes the center wavelength to vary across the detector so prior to taking data each night, we first observed a helium arc lamp installed on the 200" Hale Telescope to identify the region that is most sensitive to the 1083 nm line, and we placed our target within that region and in the same place each night for consistency. An additional effect of the center wavelength shift is that telluric OH emission lines form bright radial arcs on the detector. To calibrate this out, we constructed a background frame using a four-point dither for each night. The sky background frame from night 2 is displayed in Figure 2.1. The radial rings

are the aforementioned OH emission within our bandpass that form as arcs on the detector. For our night 1 observations, we took 90 second exposures from UT 05:03:30 to UT 10:40:11, beginning at airmass 1.237 and ending at airmass 1.207. For our night 2 observations, we took 90 second exposures from UT 05:06:57 to UT 11:01:56, beginning at airmass 1.011 and ending at airmass 2.301. Both nights reached a minimum airmass of 1.000.

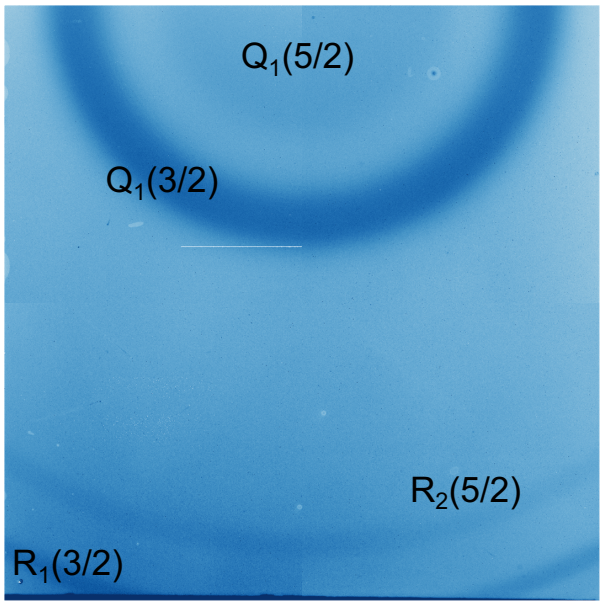

Figure 2.1: The sky background frame from night 2 generated from a four-point dither with each OH emission line labeled.

We dark-subtracted and flat-fielded all images to correct for bad pixels and detector stripping, which refers to a rectangular region that appears non-uniform on the detector arising from a few specific channels that have a different sensitivity than the others. These imperfections are visualized in Figure 2.1. The bad pixels are replaced with a median value derived from a 5 pixel by 5 pixel box centered around it. Due to the radial structure of the OH emission, we were able to correct it by median scaling the sigma-clipped science data to the dithered background frame in 10 pixel radial steps from the filter zero point (where rays pass at nor-

mal incidence) at the top of the detector. This process eliminates most of the telluric background but leaves a small residual background, which we correct for locally in our aperture photometry process. A corrected science image is shown in Figure 2.2.

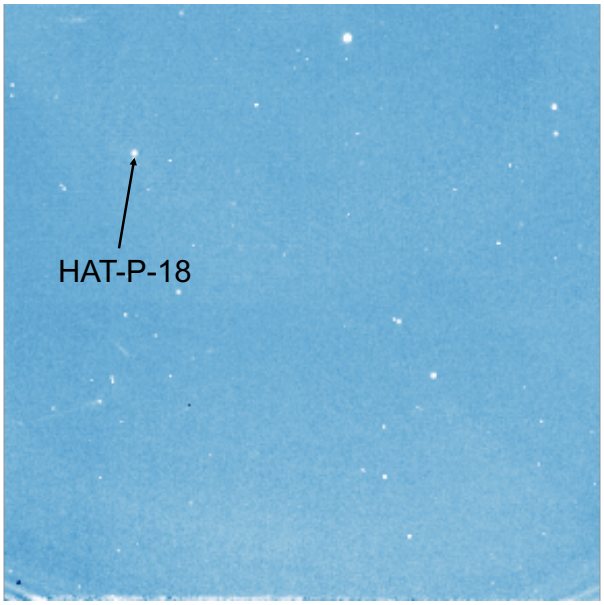

Figure 2.2: A background-corrected science frame from night 2 with our target marked.

We use these background scaling factors to correct for time-varying telluric water absoption as well. There are two water lines at 1083.57 nm and 1083.66 nm that overlap with our bandpass (shown in Figure 2.3). At the effective resolving power of our filter, these two water lines appear as a singular absorption line. Because our first night was affected by sporadic cloud coverage and significant seeing and transparency variations, we found a way to track the varying water absorption throughout the night via the OH emission lines mentioned above. The Lorentzian wing of the $Q_1(3/2)$ OH emission line at 1083.4 nm overlaps with the telluric water feature (Allart et al. 2018; Salz et al. 2018). A figure from Allart et al. (2018) is shown in Figure 2.4 showing the overlap. This means that OH

emission that originates higher in the atmosphere (>80 km, Bernath & Colin (2009)) may be absorbed by H_2O when passing through the lower atmosphere. Thus, we can track the time-varying water absorption throughout the night by dividing the time-varying flux in the water affected OH emission line, which is measured in our background scaling factors, with the unaffected OH emission lines at 1075 nm and 1078 nm. If the water variation throughout the night is significant enough to affect our photometry, we use this absorption proxy as a decorrelation parameter in our transit fits. Additionally we used HITRAN [1] to search for other contaminants, such as CH_4 and CO_2, and find no significant contamination from either molecule within our bandpass.

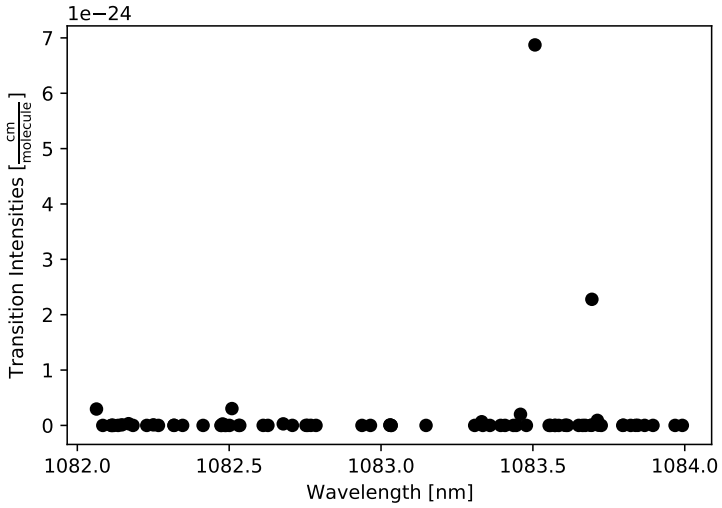

Figure 2.3: Transition intensities of the most abundant isotopologue of H_2O between 1082 and 1084 nm from the HITRAN database. The two outstanding points are the two water lines that overlap with the bandpass of our filter.

We performed aperture photometry on our target star and six comparison stars (the same ones for each night) using the package `photutils` (Bradley et al. 2020). The six comparison stars that we selected were the six brightest stars in

[1] https://hitran.org

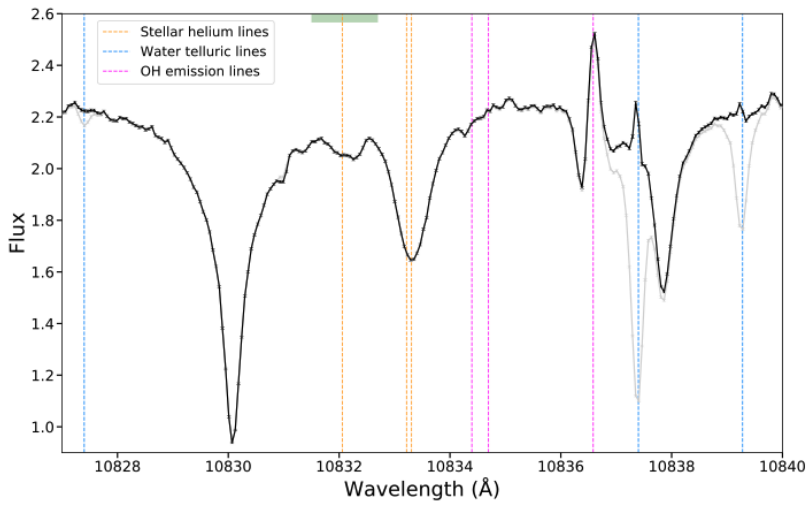

Figure 2.4: Figure S1 from Allart et al. (2018) showing their out of transit telluric corrected spectrum in black. Note the $Q_1(3/2)$ OH emission line overlapping with the telluric water line and the He I 1083 nm line denoted by the double orange dashed lines.

the field of view. We stepped through various aperture sizes in one pixel steps ranging from 3-13 pixels in radius. Using a moving median filter, we removed 3σ outliers. We find that the optimal aperture size is 7 px (1.″75) and 11 px (2.″75) in radius for night 1 and night 2, respectively. We note that this difference in optimal aperture size results from our decision to defocus on night 1 and use the diffuser on night 2. The raw light curves for each night are shown in Figure 2.5 and Figure 2.6. The raw light curves for night 1 demonstrate extreme variability throughout the night, dipping lower than a median normalized flux of 0.2, arising from the aforementioned poor weather conditions. From the raw light curves for night 2, we noticed a discontinuity in the photometry about thirty minutes into observing and a downward trend in flux in the last twenty minutes of the night. We speculate that the dip in flux may be due to light cloud coverage or instrumental effects, while the downward trend at the end of the night may have been caused by poor background subtraction from calibration. Looking at the

calibrated images corresponding to this downward trend, we noticed that the position of the target coincides with a part of an OH ring that is nonuniform, and thus the background subtraction works less effectively within that region. So we attempted to apply a `photutils` tool, `Background2D`, to generate a 2D image of the background and the background root mean square (RMS) to correct for the nonuniform background in the ring. After implementing this additional background subtraction on the science images, it appeared as if this method worked in smoothing the background of the ring, but it also increased our noise by over 10%. With this in mind, we decided to move forward with these uncorrected discrepancies left in the photometry, as the potential of being able to jointly fit the nights would allow for a better constraint on the best-fit parameters overall.

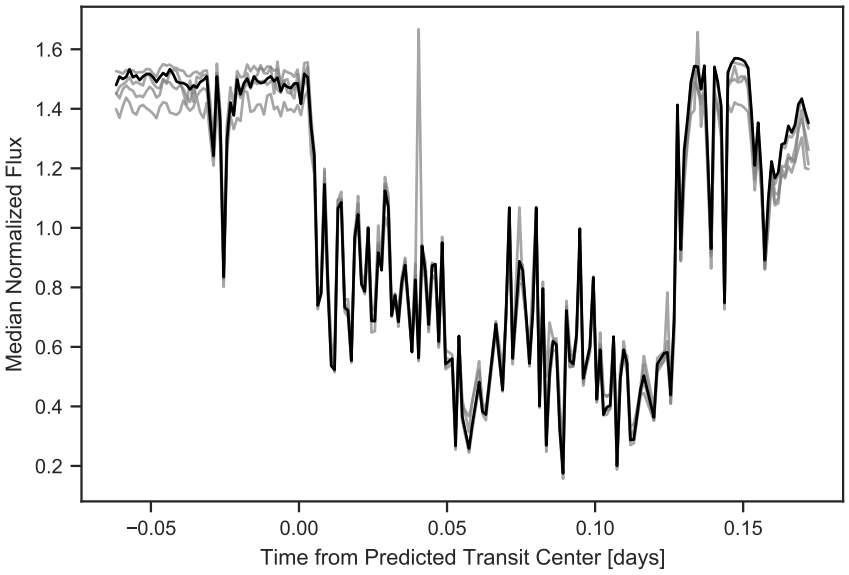

Figure 2.5: Median-normalized raw light curves of the target (in black) and its comparison stars (in grey) for WIRC night 1.

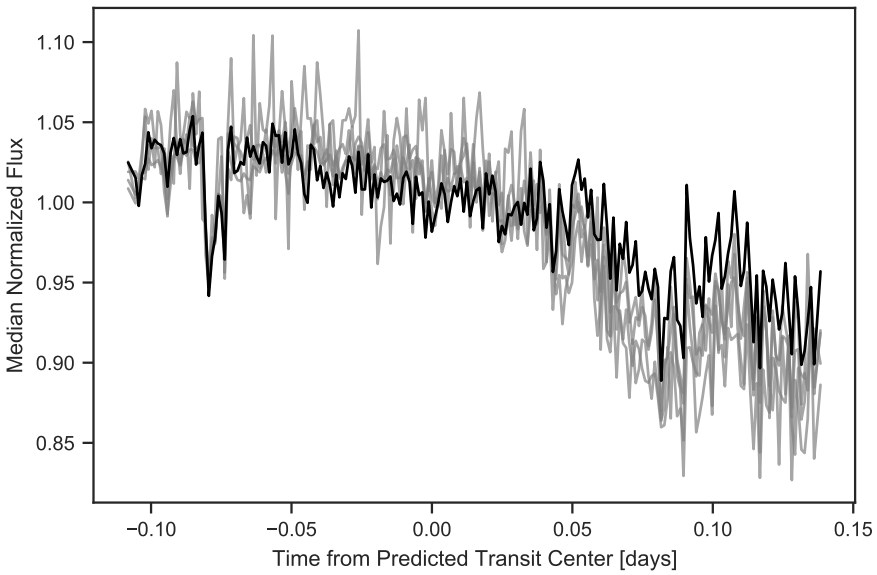

Figure 2.6: Median-normalized raw light curves of the target (in black) and its comparison stars (in grey) for WIRC night 2.

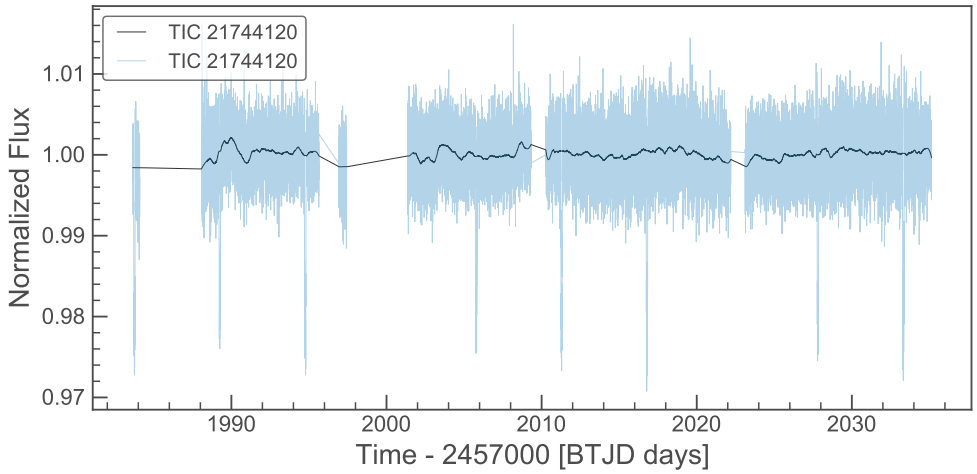

Figure 2.7: The *TESS* data in blue and the low frequency variability in black. Note that BTJD = BJD - 2457000.

2.2 *TESS* Observations

We used the 2-minute cadence *TESS* observations of HAT-P-18b obtained during Sectors 25 and 26. The target was observed by *TESS* for 51.5 days starting on May 14 2020 and June 9 2020, respectively, spanning eight total transits. We note that there are two missing transits due to the gaps in observation throughout the 51.5 days. We use this data as a comparison to our WIRC data to demonstrate that we have indeed detected excess He absorption for HAT-P-18b, and thus has an extended helium atmosphere, and to improve its ephemeris. We downloaded the Pre-search Data Conditioning Simple Aperture Photometry (PDCSAP) from the Miluski Archive for Space Telescopes (MAST) [2] via the `lightkurve` package (Lightkurve Collaboration et al. 2018). We removed low frequency variability using the Savitzky-Golay (SavGol) filter from `scipy` (Virtanen et al. 2020) and rejected 5σ outliers using a moving median filter with the transits masked. The variability estimated by the SavGol filter is shown over the TESS data in Figure 2.7. Even after these efforts, we noticed that the transit depth of the first transit around 1984 BTJD was biased due to the lack of baseline for sufficient removal of low frequency variation, so we opted to remove this transit and the minor baseline preceding it from the data. Before we proceeded, we fit the remaining seven transits and allowed each transit depth to vary while holding all other light curve parameters constant. From this fit, we noticed that the first transit of the seven that occured around 1989 BTJD had a transit depth that differed from the six other transits by greater than 1σ. This discrepancy is explained by the systematic trend along the light curve showing the largest variability, which is not being effectively corrected by the SavGol filter, and thus biasing the transit

[2] https://archive.stsci.edu

depth value. Although those first two transits may be recoverable with additional or different detrending methods, our constraint on the *TESS* transit depth using the remaining six transits is sufficiently precise to compare to the WIRC depth.

Chapter 3

Light Curve Modeling and Fitting

After we completed the data reduction and aperture photometry, we proceeded to model the transits we observed with WIRC in the 1083 nm line and the remaining six *TESS* transits in the broadband. To compensate for the high variability in weather during night 1, we aimed to be able to fit both of the WIRC datasets simultaneously to decrease the overall uncertainty and secure a detection.

3.1 Modeling with `exoplanet`

We modeled both nights of WIRC data with the corrected *TESS* photometry using the package `exoplanet` (Foreman-Mackey et al. 2021). For the WIRC light curves, we used `exoplanet`'s No U-Turn Sampler (NUTS) sampler, which uses a type of Markov chain Monte Carlo (MCMC) algorithm called Hamiltonian Monte Carlo (HMC) that takes informed steps via first-order gradient information rather than using a random walk approach (Hoffman & Gelman 2011). With the NUTS sampler, we built an instrumental noise model that consisted of a linear baseline and a linear combination of the comparison stars light curves, which corresponded to individual weights that were left as free parameters. We initially attempted to include two other decorrelation parameters for each night: the water absorption proxy (mentioned in Section 2.1) and the distance from the median centroid. To determine whether we would elect to keep a parameter in our fits, we referred to

the Bayesian Information Criterion (BIC). The BIC is founded upon the likelihood function, which aims to minimize the χ^2 of the fits. In this approach, a model with the lowest BIC value is preferred, where a $\Delta\text{BIC} < 10$ is considered to be negligible and a $\Delta\text{BIC} > 10$ is a strong indication of a better fit. For each WIRC data set, there were two comparison stars for which their posterior probability distributions coincided with zero, thus, we removed them from the fits, which resulted in a lowered BIC by 35 and 26 for night 1 and night 2, respectively. We note that these two stars are not the same for each night, which is not a surprise, since we elected to defocus the telescope on one night and use the beam-shaping diffuser on the other. We applied the water absorption proxy to both nights and found that it was only useful to include the proxy for the fits of night 1 with a ΔBIC of 17. This was expected as the weather conditions significantly impacted our observations that night. Figure 3.1 shows the night 1 absorption proxy throughout the night. Generally, the absorption proxy somewhat tracks the total flux (Figure 2.5), but demonstrates variations that do not align with the comparison stars. We kept the distance from median centroid parameter for both nights since their removal resulted in a BIC difference of less than 10. In our final systematics model, we had 15 parameters: two parameters for each of the linear baselines, four comparison stars for each dataset, the distance from median centroid for each dataset, and the absorption proxy for the first night.

3.2 Fitting with `PyMC3`

We fit a transit model along with the systematics model simultaneously. Across all three datasets, there are three common parameters: the predicted mid-transit time T_0, the period P, and the impact parameter b. Initially, we allowed each

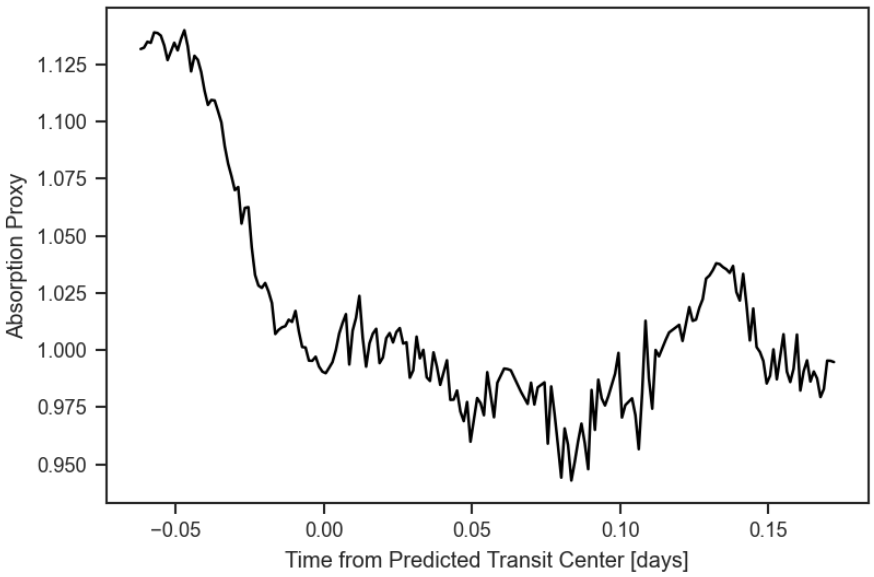

Figure 3.1: The night 1 absorption proxy vector as a function of time from predicted transit center.

night of WIRC data to have its own transit depth in the joint fit with the *TESS* photometry. The resulting transit depth for each night were within 1σ of each other (shown in Figure 3.2), indicating little epoch-to-epoch variability, thus we proceeded with fitting a single helium transit depth for both nights. For each bandpass (WIRC and *TESS*), we fit for limb darkening coefficients $[u_1, u_2]_{(\mathrm{He})}$ and $[u_1, u_2]_{(TESS)}$ and transit depths $(R_p/R_\star)^2_{(\mathrm{He})}$ and $(R_p/R_\star)^2_{(TESS)}$, which were sampled uniformly. The limb darkening coefficients are needed to correct for the fact that stars appear brighter in their centers relative to their edges, or limbs, and for our fits, we utilize an uninformative sampling approach for them from Kipping (2013) where we fit them in the interval $[0, 1]$. For each WIRC night, we also included a jitter parameter that accounted for excess noise in addition to photon noise $\log(\sigma_{\mathrm{extra}})$. We noticed that the given error bars from the PDCSAP fluxes of the TESS data did not accurately represent the true photon noise, as the

observed scatter was overestimated. So, we added a scaling factor k for the *TESS* error bars. For our transit model we had a total of 13 parameters: the predicted mid-transit time, the impact parameter, the transit depth for each bandpass (joint WIRC and *TESS*), the radius of the star, the mass of the star, two limb darkening coefficients for each bandpass, the jitter parameter for each WIRC data set, and the scaling factor for the *TESS* data set.

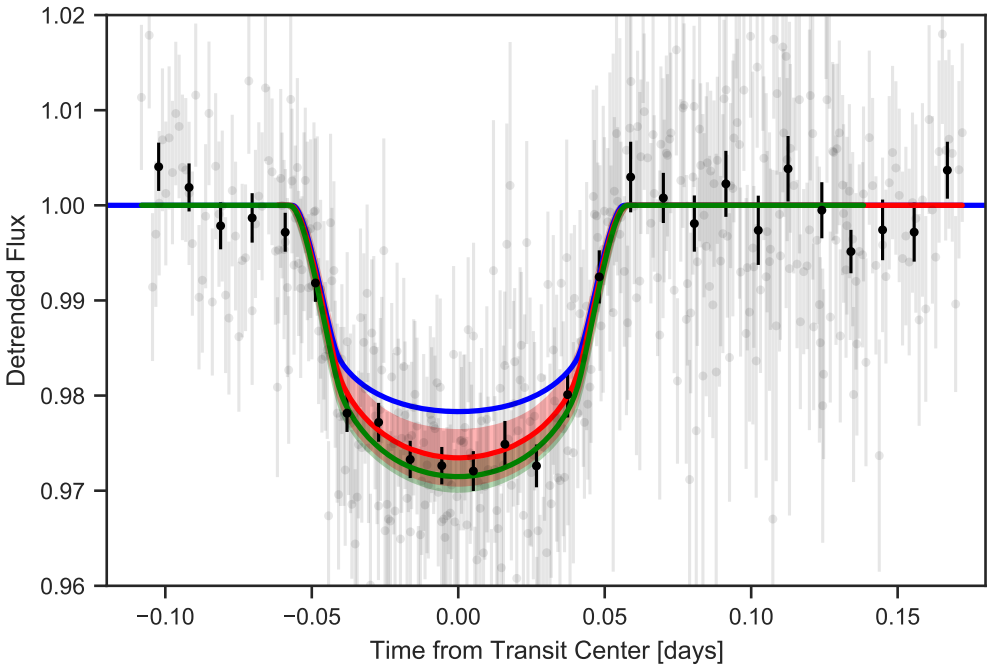

Figure 3.2: The best fit models for WIRC night 1 (green) and WIRC night 2 (red) when fit individually are overplotted with the 1σ confidence interval denoted by the shaded region. The blue is the *TESS* best fit model. The black points are the WIRC data sets binned together to a 15 minute cadence and the grey points are unbinned.

We used the NUTS in `PyMC3` to sample posterior distributions for each of our parameters in our model. We sampled 4 chains each tuned to 1500 steps (the "burn in" period) and then took 1000 draws in each chain. To determine good

Table 3.1. Priors and posteriors for joint fit to Palomar/WIRC and *TESS* data

Parameter	Prior	Posterior	Units
$(R_{\rm p}/R_\star)^2$ (He)	$\mathcal{U}(0.01, 0.25)$	2.29 ± 0.12	%
$(R_{\rm p}/R_\star)^2$ (*TESS*)	$\mathcal{U}(0.01, 0.25)$	$1.832^{+0.045}_{-0.048}$	%
P	$\mathcal{N}(5.5080291, 0.0000042)$	5.508029 ± 0.0000042	days
T_0	$\mathcal{U}(2038.5, 2039.0)$	2038.82530 ± 0.00023	$\rm BTJD_{TDB}$
b	$\mathcal{N}(0.352, 0.057)$	$0.338^{+0.047}_{-0.051}$	–
u_1 (He)	Kipping (2013)	$0.58^{+0.29}_{-0.30}$	–
u_2 (He)	Kipping (2013)	0.14 ± 0.39	–
u_1 (*TESS*)	Kipping (2013)	0.45 ± 0.16	–
u_2 (TESS)	Kipping (2013)	$0.20^{+0.30}_{-0.31}$	–
$log(\sigma_{extra})$ (night 1)	$\mathcal{U}(-4, -2)$	$-2.078^{+0.036}_{-0.038}$	–
$log(\sigma_{extra})$ (night 2)	$\mathcal{U}(-4, -2)$	$-2.40^{+0.08}_{-0.12}$	–
k (*TESS*)	$\mathcal{U}(0.5, 1.5)$	$0.8563^{+0.0037}_{-0.0036}$	–

Note. — $\rm BTJD_{TDB}$ = BJD - 2457000. We omitted the stellar parameters and the detrending weights.

convergence, we referred to the Gelman-Ruben statistic (Gelman & Rubin 1992) that compares the between-chains and within-chain variances for each model parameter, and defines that a Gelmen-Ruben statistic value less than 1.1 is indicative of convergence being reached. Thus, we are confident we achieve good convergence with a Gelman-Rubin statistic of less than 1.006 for all parameters. The priors and posteriors for the physical parameters in our model are given in Table 3.1. The joint fit and the detrended light curve, residuals, and Allan deviation plot for each night of WIRC data are displayed in Figures 3.3 and 3.4. The final combined helium and *TESS* light curves are displayed in Figure 3.5, and the posterior distributions for the model parameters are visualized in Figure 3.6.

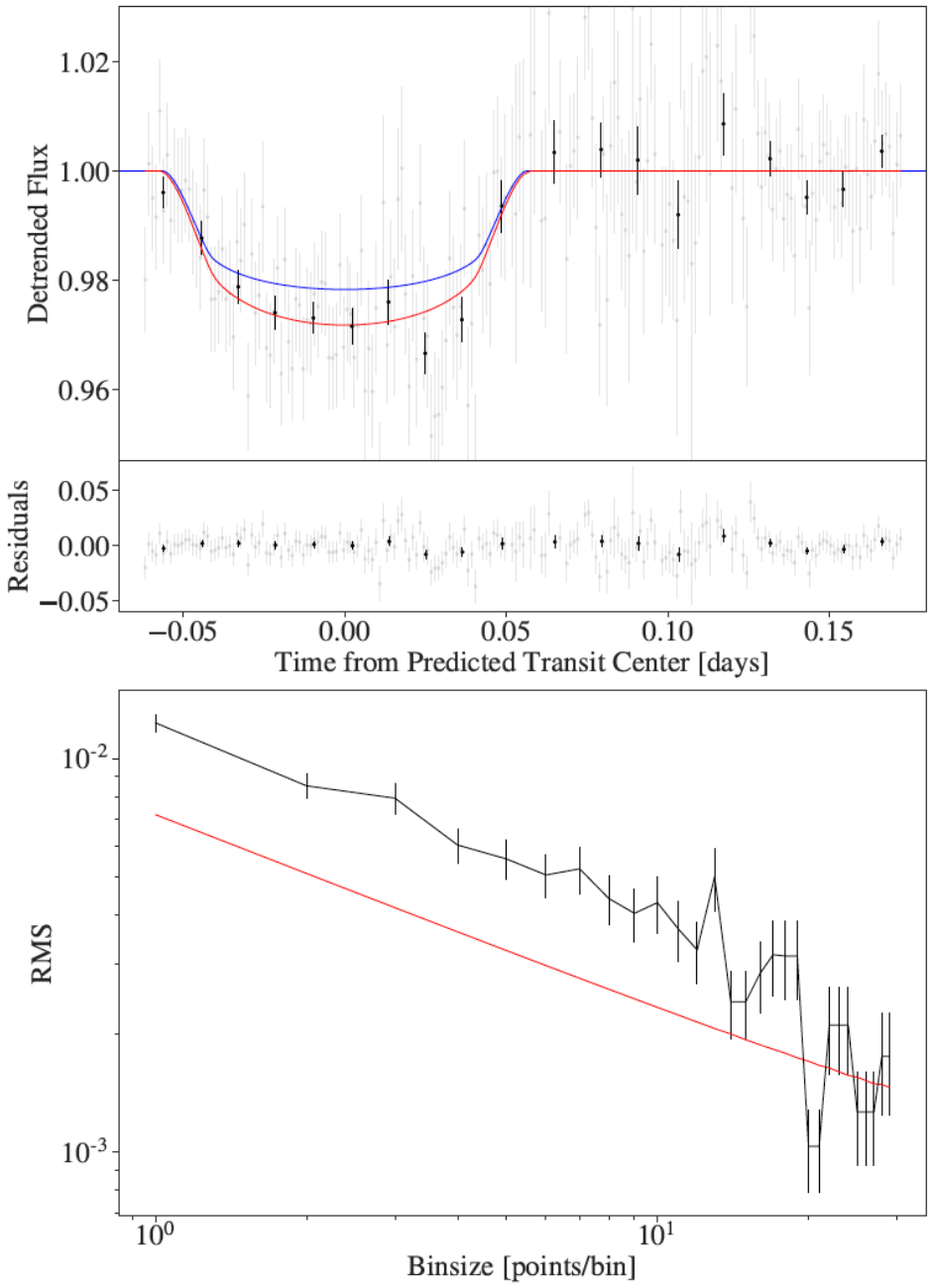

Figure 3.3: WIRC night 1 light curve with the helium model in red and the *TESS* broadband model in blue on the top and its Allan deviation plot of the residuals in black and the photon noise limit in red on the bottom.

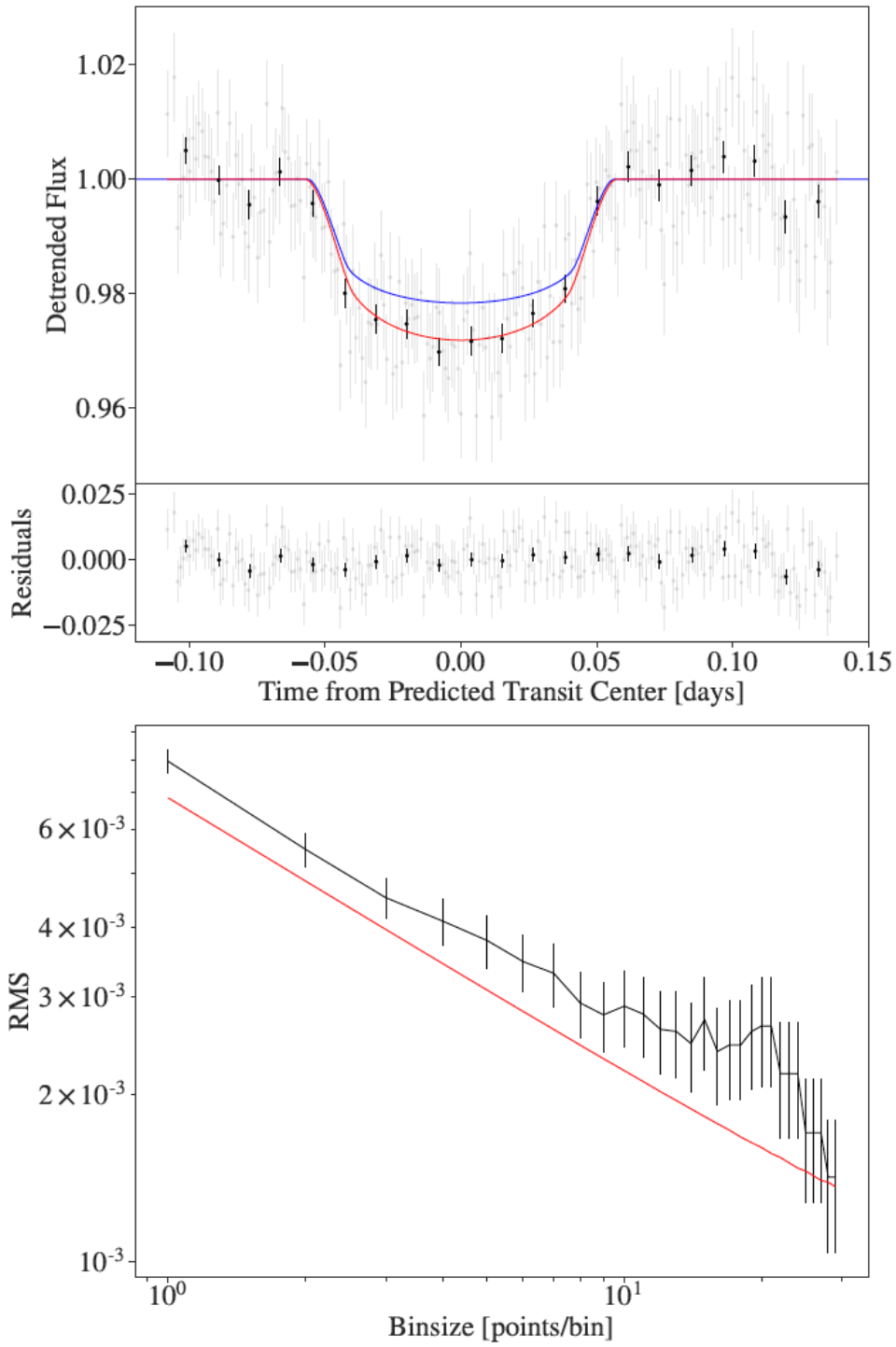

Figure 3.4: WIRC night 2 light curve with the helium model in red and the *TESS* broadband model in blue on the top and its Allan deviation plot of the residuals in black and the photon noise limit in red on the bottom.

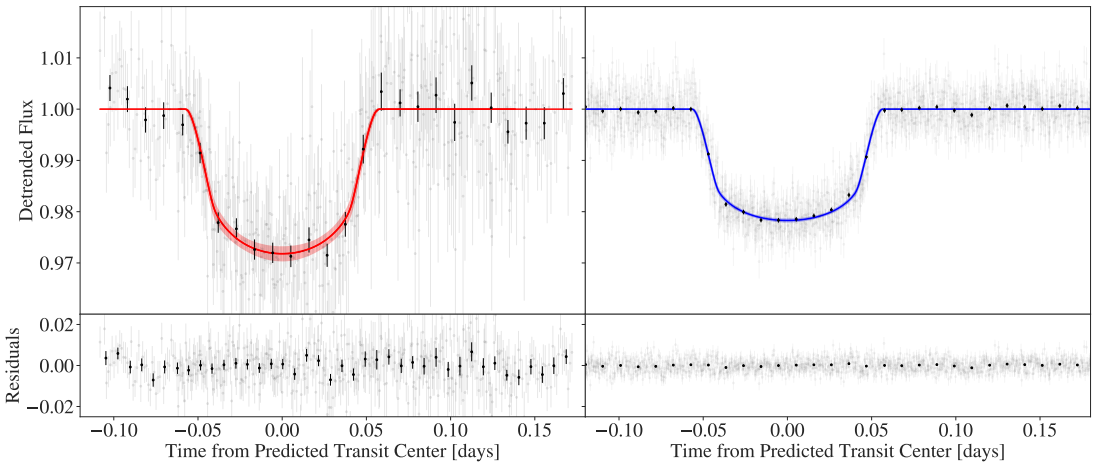

Figure 3.5: Combined transit light curves and residuals for WIRC (left) and *TESS* (right), with unbinned data in grey and binned data to a 15 minute cadence in black. The best fit models for WIRC (red) and TESS (blue) are overplotted with the 1σ confidence interval denoted by the shaded region.

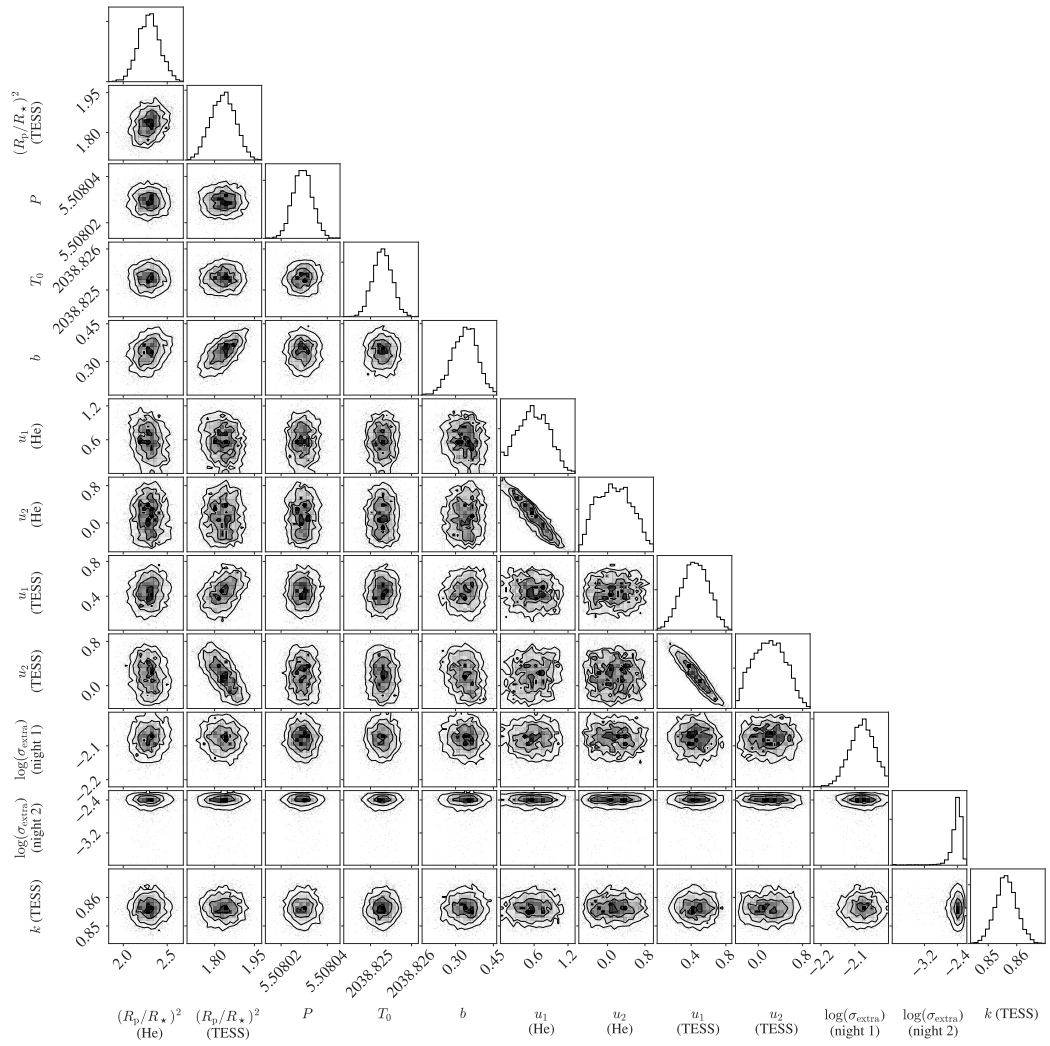

Figure 3.6: Corner plot displaying the posterior probability distributions for the joint model for HAT-P-18b. Note transit depth $(R_p/R_*)^2$ values are in %, period P is in days, and predicted mid-transit time T_0 is in $\mathrm{BTJD_{TDB}}$.

Chapter 4

Helium Results & Discussion

From our modeling and fitting, we now have transit depths from the He I ultra-narrow band and the *TESS* broadband that we can compare to determine if we have detected excess helium absorption caused by an extended helium atmosphere for HAT-P-18b.

4.1 Excess Helium Absorption for HAT-P-18b

We measured a transit depth of $2.29 \pm 0.12\%$ in the He I 1083 nm line. We compare our measurement to the *TESS* broadband transit depth of $1.832^{+0.045}_{-0.048}\%$. Our helium transit depth exceeds the TESS transit depth by $0.46 \pm 0.12\%$, or 3.9σ. The TESS bandpass of 600 nm to 1000 nm makes it a suitable broadband measurement to compare our own measurements to. Past studies of HAT-P-18b have shown that variations within this range are restricted to variations on the order of the scale height (Kirk et al. 2017), which is easily seen in the transmission spectrum of our target between about 5000 Å and 9000 Å in Figure 4.1. The scale height of a planet is defined as the physical length scale of its atmosphere and is given by

$$H = \frac{kT}{\mu g},$$

where k is the Boltzmann constant, T is the equilibrium temperature of the planet, μ is the mean molecular weight, and g is the planet's surface gravity, which is given by

$$g = \frac{GM_p}{{R_p}^2},$$

where G is the graviational constant, M_p is the mass of the planet, and R_p is the radius of the planet. For reference, Earth's scale height is about 8.5 km, while Jupiter's is about 27 km. If we assume $\mu = 2.3$ amu (which is typical for gas giants), we find that the scale height for HAT-P-18b is 537 km, which is noticeably larger than that of Earth or Jupiter. HAT-P-18b is much closer to its host star, thus it has a much higher equilibrium temperature, and a lower surface gravity since it is very similar in size to Jupiter, but much less massive. The difference between the two transit depths we measured exceeds, by an order of magnitude, the expected change in transit depth of one scale height in planet radius (0.03%) for this planet. Thus, we rule out the possibility that our observation can be explained by broadband features in the lower atmosphere. Additionally, the helium line is near an opacity minimum of water, which disfavors the broadband feature explanation a priori. So we conclude that this excess absorption is indeed due to metastable helium in the upper atmosphere of HAT-P-18b. Figure 4.2 shows the helium planet size of HAT-P-18b relative to its broadband planet size.

4.2 Constrained Atmospheric Escape Rate for HAT-P-18b

We use the model from Oklopčić & Hirata (2018), as discussed in Section 1.4, to make a joint constraint on HAT-P-18b's upper atmospheric temperature T_0

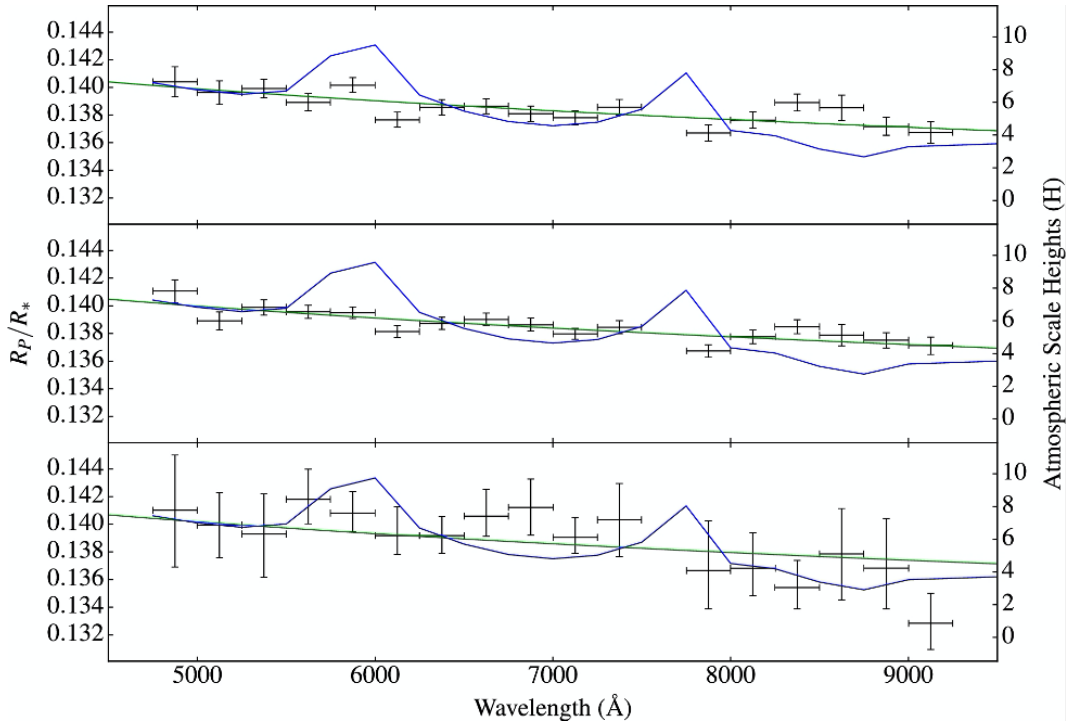

Figure 4.1: Figure 5 from Kirk et al. (2017) showing the transmission spectrum of HAT-P-18b with different methods of correcting for limb darkening and long scale trend.

and its mass loss rate $\dot{M}$ using our measured excess absorption of $0.46 \pm 0.12\%$. We first calculate the velocity and density profiles of a 90%/10% H/He 1D Parker wind as a function of the upper atmospheric temperature and mass loss rate and the level populations for helium with a UV stellar spectrum. In our case, we are using the Measurements of the Ultraviolet Spectral Characteristics of Low-mass Exoplanetary Systems (MUSCLES) UV stellar spectrum of ϵ Eridani (France et al. 2016; Loyd et al. 2016; Youngblood et al. 2016), also a K2 type star, as a stand-in for the unknown UV spectrum of our target. Adjusting for the difference in stellar radius and separation for our target system, the planet's EUV irradiance was 8 W/m^2 integrated between 5.5 Å and 911 Å. HAT-P-18b's mass loss rate in $\log(\dot{M})$ is likely between $9.7^{+0.125}_{-0.11}$ g s^{-1} ($8.3^{+2.8}_{-1.9} \times 10^{-5}$ M_J Gyr^{-1}) and $11.2^{+0.07}_{-0.12}$ g

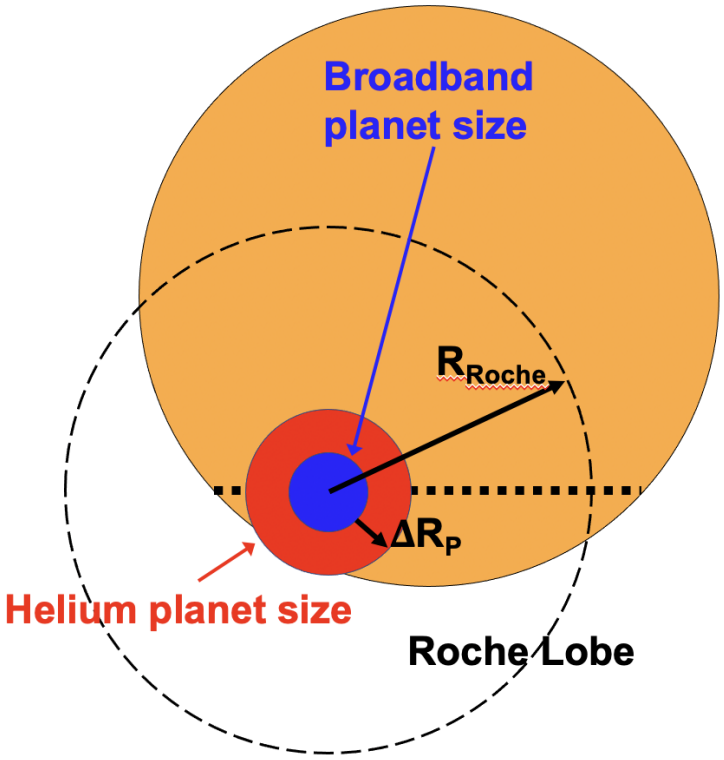

Figure 4.2: A to-scale diagram of HAT-P-18b during transit with its broadband planet size, helium planet size, and Roche Lobe size labeled. Notice that the size of the planet is effectively almost doubling in the He I bandpass.

s^{-1} ($2.63^{+0.46}_{-0.64} \times 10^{-3}$ M_J Gyr^{-1}) for upper atmospheric temperatures between 4000 and 13000 K, respectively. We note that ϵ Eridani is a much younger star with a faster rotation period compared to HAT-P-18, which could indicate that it is a much more active star, thus affecting the accuracy of our estimated mass loss rate for our target. Although HAT-P-18b is an old disk star with a slow rotation, it is a relatively active star with $\log(R'_{HK}) = 4.799$ (Piskorz et al. 2015), which is not in line with the expected age-activity scaling (Mamajek & Hillenbrand 2008). ϵ Eridani has $\log(R'_{HK}) = 4.51$, which is indeed more active than our target star, so we found an additional star in the MUSCLES survey, HD 40307, that is a K2.5V star with $\log(R'_{HK}) = 4.99$ (Mayor et al. 2009), placing it on the other

end of HAT-P-18's activity in relation to ϵ Eridani. Figure 4.3 shows the incident flux for ϵ Eridani and HD 40307 at the orbital distance of HAT-P-18b. We can notice that the spectra are broadly similar down to about 100 Å. Although ϵ Eridani has a much stronger X-ray flux, it does not affect the metastable helium population (and thus the inferred mass loss) because X-rays have an exceptionally low cross-section to helium ionization (in the high energy-limit, the cross section is proportional to $E^{-7/2}$). The relevant quantity in the photoionization model is the flux-averaged cross-section (Oklopčić & Hirata 2018), and the X-ray flux has a very small contribution to this. The flux between 100 Å and 504 Å, which populates the metastable helium via ionization and subsequent recombination, and between 500 Å and 2600 Å, which depopulates metastable helium via direct ionization, is a factor of about 2.5 greater for ϵ Eridani. However, the overall population of metastable helium is controlled by the ratio of these flux ranges (Oklopčić 2019), which is quite similar between the two spectra. With this in mind, we reran the model using the spectrum of HD 40307 and determined the best-fit value in $\log(\dot{M})$ at 4000 K is $9.60^{+0.11}_{-0.12}$ g s^{-1} and at 13000 K is $11.20^{+0.12}_{-0.11}$ g s^{-1}. The values between the two stars are quite similar, which agrees with our expectation due to their respective mid-UV to EUV flux ratios, thus we stand by our initial decision to use ϵ Eridani as a stand-in for HAT-P-18b. Our estimated mass loss rate translates to HAT-P-18b losing less than 2% of its mass per Gigayear, which is typical for close-in gas giants with other helium outflow detections having mass loss rates less than 5% per Gigayear (Allart et al. 2018; Mansfield et al. 2018; Spake et al. 2018; Alonso-Floriano et al. 2019). The results of the model are shown in Figure 4.4. To ensure our estimated mass loss rates are energetically realistic, we calculated an energy-limited mass loss rate for the planet (Murray-Clay et al. 2009):

$$\dot{M} = \frac{\varepsilon \pi R_{\rm p}^3 F_{\rm XUV}}{G M_{\rm p}} \approx 4 \times 10^{10} \text{ g s}^{-1},$$

where we use an efficiency parameter of $\varepsilon = 0.1$ and the EUV irradiance from above. This estimation agrees with our mass loss rates from the 1D Parker wind model, demonstrating that our measurement yields an expected mass loss rate for the system.

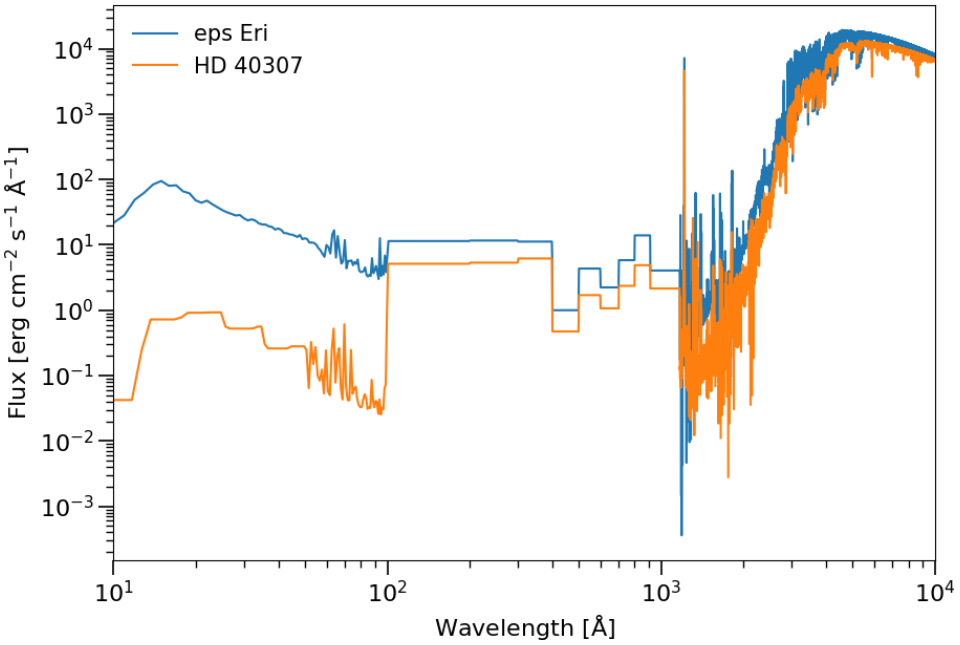

Figure 4.3: The incident flux for ϵ Eridani (in blue) and HD 40307 (in orange). Notice the largely course data between 100 Å and 1000 Å region, or the EUV range, due to the local interstellar medium, and the strong Lyα emission line at 1215 Å. Figure made by Antonija Oklopčić.

We note a strong degeneracy between the upper atmospheric temperature and the mass loss rate arising from the dependence of the outflow velocity along with the complex changes in the density profile with the temperature and mass loss rate. Although this degeneracy could be somewhat resolved by a precise line shape

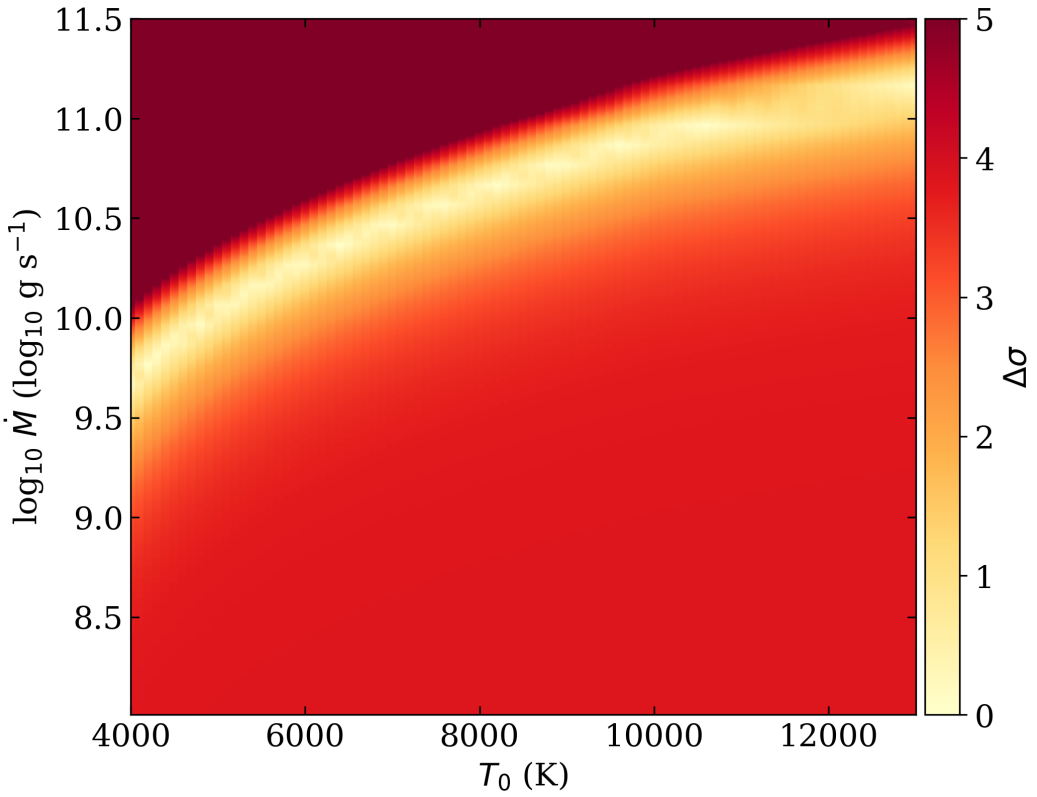

Figure 4.4: Atmospheric mass loss model for HAT-P-18b. Each point is a different mass loss model corresponding to specific T_0 and $\dot{M}$ values with the lighter regions indicating where the model matches our observed excess absorption best. Figure made by Antonija Oklopčić.

measurement, which we do not measure in our observations, spectrographs on all but the largest telescopes would have trouble resolving the line shape precisely enough due to the faintness of the target. Additionally, our helium light curve is symmetric across our best-fit mid-transit time. But we do not rule out the possibility of an extended egress, which would suggest a trailing helium tail for the target, since we lack the precision required to significantly make a conclusion.

4.3 Hot Giant Planets Orbiting K-Type Stars

As discussed briefly in Section 1.3.2, there have been six other unique He I detections thus far, making HAT-P-18b the seventh planet with excess helium absorption in its atmosphere. Of these seven planets, five orbit K-type stars, WASP-107b, WASP-69b, HD 189733b, HAT-P-11b, and HAT-P-18b, while the other two orbit a G-type star (HD 209458b) and an M-type star (GJ 3470b). These planets orbit at relatively similar semi-major axes ranging between 0.03106 AU (HD 189733 b) and 0.0559 AU (HAT-P-18b), but demonstrate various outflow strengths. More specifically, there is a noticeable difference between each planet's $\Delta R_{\rm p}$ to $R_{\rm Roche}$ ratio, where $\Delta R_{\rm p}$ is the difference between the measured He I planet radius and the broadband planet radius and $R_{\rm Roche}$ is the radius of the Roche lobe of the planet. This is shown in Figure 4.5. Although the sample of planets with detected helium absorption is still too small to establish any definitive trends, it appears that planets that are further away from their host stars demonstrate stronger helium outflows. This is counterintuitive as we expect planets that are closer to their host stars to experience increased radiation relative to planets that orbit further, thus to have stronger outflow signatures. Some possible explanations for the potential trend we are beginning to see in this population of planets include that their upper atmospheres may be mostly ionized, transforming He into He^+ (Oklopčić 2019), their atmospheres are being confined by their host star's stellar wind (Vidotto & Cleary 2020), or the planetary magnetic fields of the closer-in planets are shepherding their outflows. As more helium detections are made, the better we will be able to characterize this trend and the reasons behind it.

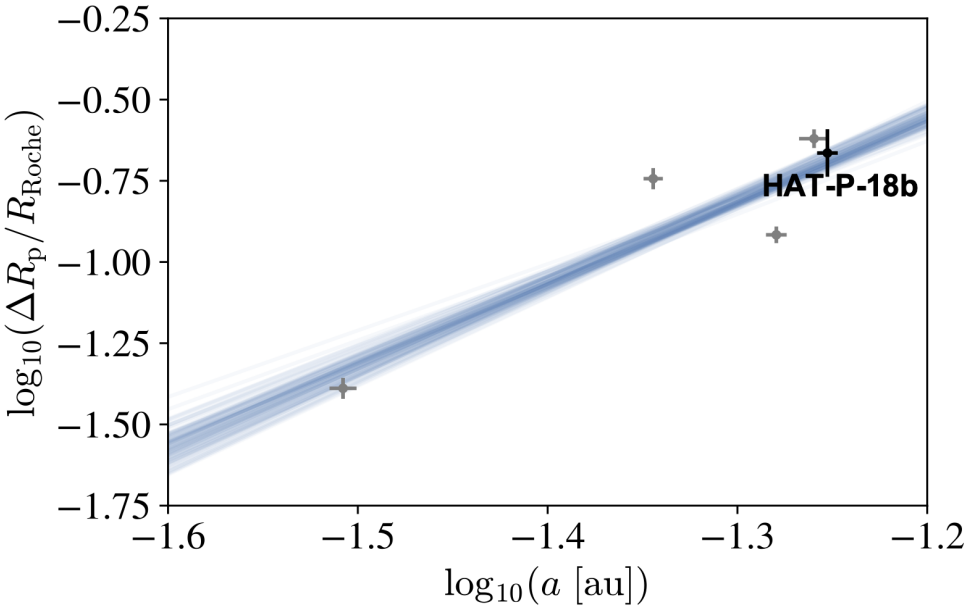

Figure 4.5: The population of planets with detected helium absorption that orbit K-type stars are shown in grey with HAT-P-18b in black. The blue shaded lines are best-fit lines through the data accounting for error.

4.4 HAT-P-18b Direct Comparison to WASP-107b

Of the handful of planets with excess helium absorption in their atmospheres, WASP-107b is the most similar to HAT-P-18b with a radius of $0.94R_{\rm J}$, mass of $0.12M_{\rm J}$, semi-major axis of 0.055 AU, and an equilibrium temperature of 770 K (Anderson et al. 2017). Their planet properties are shown side by side in Table 4.1. As mentioned previously, we do not measure the helium line shape for HAT-P-18b, but if we assume that it has a similar line shape to WASP-107b, we can convert our measured helium transit depth to estimate a line depth of $4.5 \pm 1.3\%$. Although these planets have very similar parameters, our predicted line depth for HAT-P-18b is significantly smaller than WASP-107b's measured line depth of $7.26 \pm 0.24\%$ (Allart et al. 2019; Kirk et al. 2020). This distinction may arise from

Table 4.1. HAT-P-18b and WASP-107b Planet Properties

Property	HAT-P-18b	WASP-107b	Units
Discovery Year	2011	2017	–
Host Star Spectral Type	K2	K6	–
M_p	0.196 ± 0.008	0.12 ± 0.01	M_J
R_p	0.947 ± 0.044	0.94 ± 0.02	R_J
ρ	0.286 ± 0.042	0.19 ± 0.03	g cm^{-3}
a	0.0559 ± 0.0007	0.055 ± 0.001	AU
T_{eq}	841 ± 15	770 ± 60	K

Note. — M_J and R_J are the mass and radius of Jupiter, respectively. The planet properties for HAT-P-18b are from Esposito et al. (2014) and WASP-107b are from Anderson et al. (2017).

the difference in gravitational potential between the two planets. WASP-107b has a smaller gravitational potential than HAT-P-18b, and recently, Piaulet et al. (2021) revealed that the mass of WASP-107b may be even lower than previously determined. Additionally, the difference in EUV flux spectra between HAT-P-18 (a K2 star) and WASP-107 (a K6 star) may explain the difference in helium line depth. Thus, further analysis on these two systems may be useful for constraining the mechanisms of metastable helium outflow.

In this chapter, we presented our measured helium transit depth of HAT-P-18b, which we translated into a present-day atmospheric mass loss rate, but we remain in the dark in regards to the structure and flow of the mass loss. Further studies of the system may illuminate if the escape is symmetrical across the planet or if the mass loss varies with time. Both of these open questions can be addressed by using the 3D hydrodynamic code, `Athena Æ`, which we explore in the following

chapter.

Chapter 5

Atmosphere Modeling

Our detection of the extended helium atmosphere of HAT-P-18b motivated us to explore how close-in gas giant planet atmospheres vary in time and depend on their host star's stellar wind. This curiosity led us to modeling the atmosphere of a close-in gas giant using McCann et al. (2019)'s `Athena Æ`.

5.1 Introduction to `Athena Æ`

In this work, we make use of `Athena Æ` (previously mentioned in Section 1.4), which is founded upon `Athena` (Stone et al. 2008), a code to solve astrophysics magnetohydrodynamic (MHD) problems. Granted, `Athena` was not the first algorithm to solve these sorts of problems, but it expands upon the established MHD codes by adding useful techniques such as static and adaptive mesh refinement (SMR and AMR). These techniques, which are able to resolve a big range in length scales with grid-based methods, were first shown to be beneficial for solving MHD problems in Berger & Colella (1989) in which they demonstrated that enforcing conservation at internal boundaries between fine and course meshes is needed to ensure no false reflections occured in calculations. With these improvements, `Athena` is a useful tool for studying the interstellar medium (ISM), star formation, and accretion flows.

`Athena Æ` builds upon `Athena` in order to make 3D radiative hydrodynamic

simulations of tidally-locked hydrogen atmospheres that receive copious amounts of ionizing extreme-ultraviolet flux in different stellar environments in the case of a low planetary magnetic field. McCann et al. (2019) make a handful of changes to better apply it to the escaping atmospheres of close-in exoplanets. First, they added a first-order flux correction to the corner transport upwind (CTU) integrator (Colella 1990; Saltzman 1994). An integrator specifies how each time-averaged flux is calculated at an interface in each dimension. This prevents negative density or pressure values by identifying boundaries with negative values and recalculating at each boundary using a more stable, first-order flux. Second, they altered the original shearing box feature with a Coriolis force without a centrifugal term, in order to be able to use non-periodic boundary conditions. Additionally, they changed the boundary conditions to dipole boundary conditions to prevent issues with flow bending near boundaries. They added a method that is applied at SMR boundaries in order to maintain prolonged values as positive when there are large density jumps from the expansion of the planetary atmosphere when it is radiatively cooling during the early part of the simulation. Lastly, they applied minor improvements to the temperature calculation in the ionization package to improve accuracy. With these alterations, the code is now able to model the escaping atmospheres of exoplanets exposed to their host star's intense radiation.

5.2 Parameters

To use `Athena Æ` for a specific planetary environment, one must define the planet's mass, $M_{\rm p}$, radius, $R_{\rm p}$, temperature at $R_{\rm p}$, $T_{\rm p}$, and semi-major axis, a. Additionally, one is able to define stellar parameters, such as the mass, $M_\star$, radius, $R_\star$, ionizing flux, F_0, and photon energy, $h\nu$. Other parameters that may be al-

tered are related to the stellar wind, namely, its reference radius, $r_{\star,0}$, temperature at $r_{\star,0}$, $T_{\star,0}$, velocity at $r_{\star,0}$, $v_{\star,0}$, and proton number density at $r_{\star,0}$, $n_{\star,0}$.

Within `Athena Æ`, there are three possible simulations to run: *Rogue*, *Tidal*, and *Rotating*. The difference between each option is the bounds of the problem and the specific forces explored. For example, the *Rogue* simulations are made within a $(50R_{\rm p})^3$ box centered on the planet without a stellar wind, while the *Tidal* simulations take place in a box that is $25R_{\rm p}$ larger in the negative x-axis pointing towards the star including a stellar wind and non-inertial forces from the planet's orbit, and the *Rotating* simulations add $25R_{\rm p}$ to both the positive and negative y-axes of the *Tidal* simulations with the presence of the Coriolis force.

The computational expense of these simulations are dependent on which of the three simulations chosen, in addition to the strength of the stellar wind applied. The run time of the simulation goes up with the size of the domain of the simulation and the increase of stellar wind strength. According to McCann et al. (2019), the least computationally expensive set-up would be to run a *Rogue* simulation without a stellar wind (estimated to be on the order of a couple of days), while the most computationally expensive would be a *Rotating* simulation with a strong stellar wind (estimated to be on the order of a month). We note that these computation timescales correspond to the set-up that McCann et al. (2019) uses and that they do not necessarily align with our set-up or other clusters.

5.3 Test Run

5.3.1 Set-Up

Prior to changing any parameters, we attempted to replicate the test case presented in McCann et al. (2019), which applies an intermediate stellar wind in the *Rotating* simulation case with the largest grid. They set $M_{\rm p} = 5.0 \times 10^{29}$ g $\approx M_{\rm S}$, where $M_{\rm S}$ is the mass of Saturn, $R_{\rm p} = 1.5 \times 10^{10}$ cm $\approx 2R_{\rm J}$, where $R_{\rm J}$ is the radius of Jupiter, $T_{\rm p} = 1100$ K, and $a = 10^{12}$ cm ≈ 0.07 au. These parameters correspond to an orbital period P of 6.4 days. These specific parameters were chosen such as to increase the scale height of the planet by minimizing the planet's surface gravity g at 148 cm s^{-2}. Additionally, these parameters are roughly similar to the conditions of WASP-17b. The simulation run time is set to 2×10^6 seconds $\approx$ 23 days (corresponding to $\sim$ 3.5 orbits), which does not reflect the actual time the computation takes to run. They use the Sun's parameters as the stellar parameters for the problem with $M_\star = M_\odot = 1.989 \times 10^{33}$ g and $R_\star = R_\odot = 6.957 \times 10^{10}$ cm. They use an ionizing flux of $F_\infty = 2 \times 10^{13}$ cm^{-2} s^{-1}, which is similar to the Sun's EUV flux at 0.05 au, and an $h\nu = 16$ eV. Lastly, they define the parameters of the stellar wind as $n_{\star,0} = 1.5 \times 10^4$ cm^{-3}, $T_\star = 1.35 \times 10^6$ K, and $v_\star = 200$ km s^{-1}. These correspond to a stellar wind strength of 1.3×10^{-15} M$_\odot$ yr^{-1}.

5.3.2 Running `Athena Æ` on Wesleyan's High Performance Computing Cluster (HPCC)

To run such a computationally expensive simulation, one must utilize a High Performance Computing Cluster (HPCC) because `Athena Æ` is parallelized via the

Message Passing Interface [1], which cannot be performed on a singular computer. Parallel computing is defined as a type of computation where calculations or executions of processes are done simultaneously and MPI is a standardized Application Programming Interface (API) that can perform such computing. Fortunately, the Wesleyan Natural Sciences and Mathematics Division has its own HPCC, which is what we use to run `Athena Æ` for this project. The HPCC is managed by Henk Meij and if one is interested in using the cluster, contact him to obtain an account.

Once an account is obtained, one can access the cluster through `ssh` while connected to either Wesleyan's internet network or the Wesleyan VPN. First, one must download `Athena Æ` to their home directory. Then, run GNU's `autoconf` from the top directory (`athena_ae`) to create a configure file that is compatible with one's specific setup. Next, in the terminal, run a configure executable specifying the inputs needed for the problem. We used the line on the `Athena Æ` GitLab [2]:

```
./configure --with-problem=planet_ae --with-gas=hydro
--enable-ion-radiation --enable-ion-plane --with-flux=roe
--enable-h-correction --enable-fofc --with-nscalars=1
--enable-mpirun --enable-smr --enable-shearing-box
```

Lastly, one can build `Athena Æ` with the command `make all`. Once that is completed, the environment is ready to run simulations.

Unlike running code in the terminal on a personal machine, the cluster requires the submission of a job to run code via the scheduler, which allocates the work to various cores within the cluster. In order to submit a job, one will need to make a submission script that includes the commands needed to complete the job and the

[1] https://www.open-mpi.org
[2] https://gitlab.com/athena$_a$e/*athena$_a$e*

invocation of the code. To create a submission script, we were heavily guided by Kevin Flaherty's Cluster Guide [3] on GitHub. It is an incredibly helpful resource and we suggest consulting his guide for further details. Below, we show the script used to submit an `Athena Æ` job to the HPCC.

```
#! /bin/bash
rm -f err out
#BSUB -n 36
#BSUB -R 'span[host=1]'
#BSUB -q mw128
#BSUB -J test
#BSUB -o out
#BSUB -e err
#BSUB -N

export PATH=/share/apps/CENTOS6/openmpi/3.1.3/bin:$PATH
export LD_LIBRARY_PATH=/share/apps/CENTOS6/openmpi/3.1.3/ \
lib:$LD_LIBRARY_PATH

mpirun -n 24 /share/apps/CENTOS6/athena/yes-mpi/
athena_ae-release-1.0/bin/athena \
 -d $HOME/athena/sim/Rotating_15e3 \
 -i $HOME/athena/tst/planet/athinput.planet_ae_large \
 > result.$LSB_JOBID

 cp results.$LSB_JOBID $HOME
```

[3] https://github.com/kevin-flaherty/ALMA-Disk-Code/blob/master/cluster_guide.pdf

The first line specifies that the shell script is setup in bash. The second line deletes any previous iteration of `err` and `out` files. The third specifies the amount of cores for the job (in this case, 36). Next, we specify that all the cores should come from a single node. Then, we specify which queue the scheduler should send the code. The next three lines provide the name of the job, and the names for the output and error files. Lastly, we request the scheduler to send us (the user) an email when the code errors out or finishes. The next block of code gives the path to the directory where the code is located since the job will not be completed within our own home directory, but rather a working directory that is created when the job is submitted, and it sets up the software environment needed for our code. The next two blocks call the code and copies the results back to our home directory.

To submit this job to the scheduler, use the command `bsub < scriptname`, where scriptname is the name allocated to one's script. There are various ways to check on the code such as through the commands `bjobs`, `bhist`, or `lsload specific_node`, where specific node is the login node where the job was submitted.

This test run allowed us to fully realize what the HPCC is exactly capable of handling and encouraged us to take a deeper look under the hood of `Athena Æ`. As discussed, this code is computationally expensive, even in the case that needs the least amount of work, the code requires a specific set-up that aligns with the physical CPU core count of the cluster. Of the currently existing queues within the HPCC, the `mw128` queue offers the highest number of physical CPU cores at 24. This physical CPU core count restricts our ability to run any `Athena Æ` simulation in its entirety because the code is split into 6 domain blocks, which each specify a certain amount of zones per direction (x, y, and z) and number of grids to use with MPI. To calculate the physical core count needed to run the

code in its entirety, we sum the products of each domain grid size,

$$n_{\text{grid size}_1} \times n_{\text{grid size}_2} \times n_{\text{grid size}_3}.$$

With our 24 physical CPU core count limitation in mind, the best we can do on the HPCC is to only use the first three domains with their grid sizes set to $2 \times 2 \times 2$, which brings us to a 24 physical CPU core count. This severely limits our ability to obtain simulation results that exactly match the test case discussed in McCann et al. (2019).

Following many weeks of trial and error of running the code on the HPCC, we realized that the test case we were attempting to reproduce with the input file `athinput.planet_ae_large` was not suitable for the cluster. It did not respond well to the `mpirun` command, which meant if we wanted to run it, we would need to run it sans parallelization. In that case, the code would take over a year to complete, which was not feasible, not only for our timeline, but in general. Before we terminated this run, the simulation produced some output files. It is worth noting that we did not restrict the domains for this run, which meant that these output files enabled us to obtain a better idea of what exactly we were omitting from future runs where we did place domain restrictions. The output files of `Athena Æ` are in the form of `.vtk`[4] files. To visualize our data, we used an application called Paraview [5]. Although it was not able to complete a full run, it did produce five `.vtk` files at the first time step of $t = 0$ at each level ranging from zero to four. These outputs were particularly illuminating because we were able to determine which domains are responsible for specific regions in the simulation. We find that each level builds upon the planet's atmosphere with level

[4]https://vtk.org/Wiki/Main_Page
[5]https://www.paraview.org

0 corresponding to the entire core of the planet, and each level from there (1, 2, 3, and 4) is an added layer of the atmosphere. Additionally, each level has its own level of refinement, so as the level increases, the finer the mesh scale. The density of each level is plotted in three dimensions in Figure 5.1. At each snapshot shown, we built on the previous meaning that the image labeled as "Level 1" includes both levels 0 and 1, the image labeled "Level 2" includes levels 0, 1, and 2, and so on.

Since we could not proceed with the large simulation on the HPCC, we turned to the other planet input files, `athinput.planet_ae_medium` and `athinput.planet_ae_small`. The difference between the three is the number of zones in each domain for each input file, with the large corresponding to an increased amount of zones relative to the medium, which has a smaller number of zones than the large, but a larger number of zones than the small. The medium planet simulation also did not run, but fortunately, the small planet simulation ran with the configuration of each grid size (which there are three of) set to two and the amount of domains used restricted to three. We decided to utilize the small simulation for our science case below.

5.4 Small Simulation Preliminary Results

The process of familiarizing ourselves with Wesleyan's HPCC, the code, `Athena Æ` itself, and putting the two together took a longer period of time than we initially estimated, thus we only show preliminary results from our first successful run in this section. We began this run on April 5 2021, and it completed on April 16 2021, bringing the total computation time to be about 11 days. This run time is somewhat shorter than it would have been if we were able to use all the domains

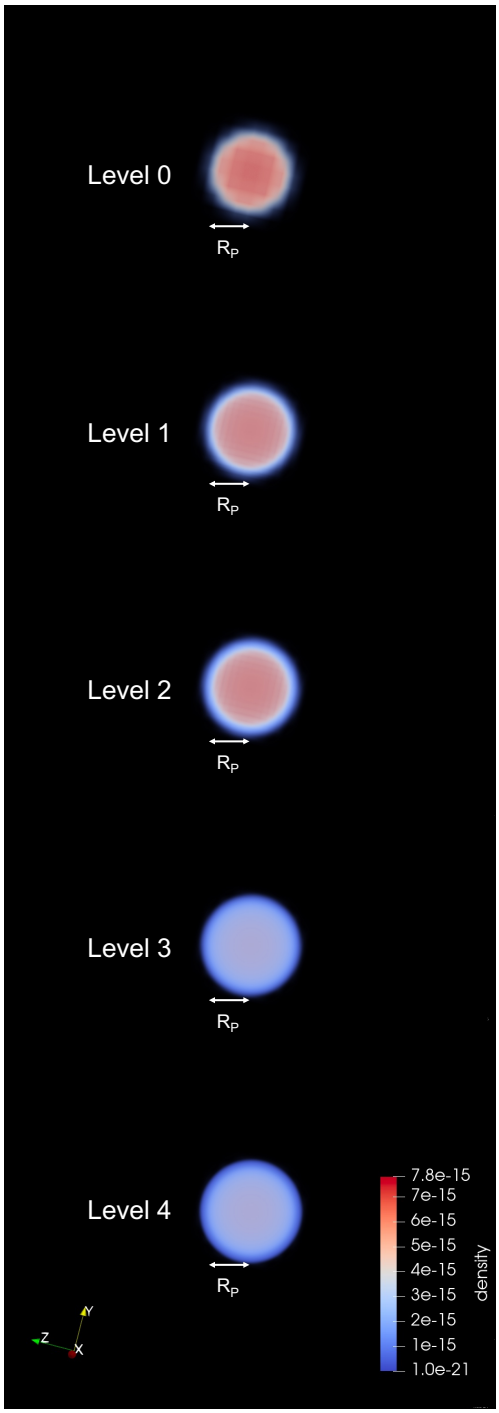

Figure 5.1: The output from our initial run using the large simulation case for $t = 0$, with each level labeled. The direction of the host star is out of the page towards the reader. The density scale is shown in units of g cm^{-3}. Recall that the radius of the planet R_p is equivalent to 2 Jupiter radii.

within the code, so a complete successful run would have taken an additional amount of time. Due to our restriction to only the first three domains, we only modeled levels 0, 1, and 2, which meant that we excluded levels 3 and 4, thus we were unable to model additional layers of the atmosphere that may be crucial for understanding how atmospheric symmetry and variability change with time.

At the completion of the run, it had produced a total of 4623 `.vtk` files with each time step having 23 `.vtk` files that are responsible for building the planet and its atmosphere. `.vtk` files can be merged using the `join_vtk.c` code located in the `athena_ae/vis/vtk` directory. So we merged all `.vtk` files with the same time step and level, resulting in the production of three `.vtk` files for each time step, totaling the amount of `.vtk` files for the run to 603. Each `.vtk` file is comprised of three dimensional data for many parameters such as density, flux, momentum, rate of ionized hydrogen recombining, ionizing, and advecting, temperature, and total energy at a specific time in the simulation.

For our preliminary analysis, we will primarily focus on several key specific time steps, namely, at the very beginning of the simulation at $t = 0$, a handful of times ranging from 1% ($t = 2.0000842 \times 10^4$ s) and 5% ($t = 1.000028 \times 10^5$ s) of the run time which corresponds to within less than a fifth of an orbit, and 25% of the way through at $t = 5.000108 \times 10^5$ s, which corresponds to ~ 1 orbit. Throughout the simulation, we noticed that the density structure of the planet and its atmosphere remain largely similar. At $t = 0$, there is not much to note other than that the three dimensional image of density looks exactly the same as the level 2 snapshot in Figure 5.1. This is expected as the simulation is merely building the planet and its atmosphere at the beginning.

The most change occurs in the first 5% of the simulation, which corresponds to the first 1.000028×10^5 seconds, or $\sim$17 hours. At 1% of the simulation at

$t = 2.0000842 \times 10^4$ s, we noticed that a particular parameter, the rate of ionized hydrogen recombining with electrons $\dot{n}$, began to develop. The rate of hydrogen recombination provides us a window into the changing atmosphere of the planet due to the ionized radiation coming from the stellar wind of the host star. In particular, the stellar wind is causing the planet's atmosphere to be asymmetric, with only the day side of the planet (which faces the negative x direction) demonstrating hydrogen recombination. Figure 5.2 shows a 3D snapshot of $\dot{n}$ in 1% increments from 1% to 5%. As time increases, the rate of recombination increases, and the space that it occurs expands. We can take a closer look by inserting a line through the x axis with $y = z = 0$ of the 3D simulation and extracting the data along it for each time shown in Figure 5.2. We plotted the rates of recombining hydrogen atoms on the y axis as a function of the x direction in units of the radius of the planet R_p in Figure 5.3. In these first 17 hours, the rates of recombination peaks around the same distance from the planet at $x = -1.03R_p$, but increases gradually until it reaches $\dot{n} = 746.96$ cm^{-3} s^{-1} at 5%, or 1.000028×10^5 seconds. This peak motivated us to additionally plot the rates of recombination along the z axis at $x = -1.03R_p$ while still maintaining $y = 0$, which in Figure 5.4. This shows that the rates of recombination are symmetric across this specific line in the simulation. An interesting result is that the rate of recombination has a less rapid increase in the z direction and begins closer to the planet. This makes sense because the host star is along the x direction, so the rays of stellar radiation are not impacting the z direction head on. We notice that the peak of the rate of recombination at $t = 1.000028 \times 10^5$ s remains largely constant throughout the remainder of the simulation.

For further evidence that the rate of recombination reached its peak earlier in the run, we present a snapshot of the planet and its atmosphere a quarter

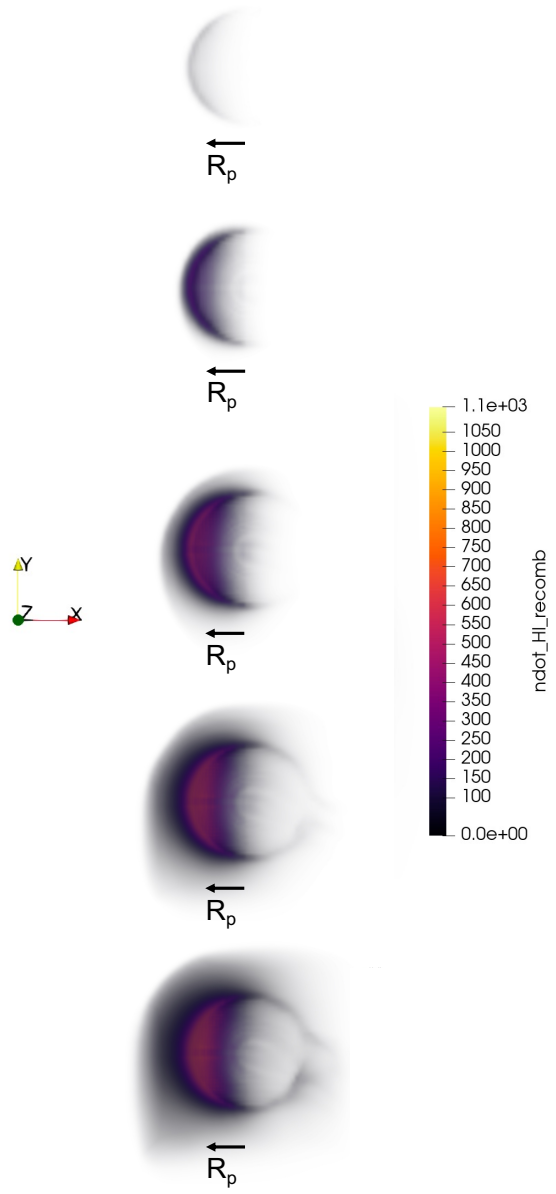

Figure 5.2: Snapshots of the rate of hydrogen atoms recombining with electrons in the atmosphere of the planet. Beginning from the top, each figure corresponds to $t = 2.000842 \times 10^4$ s, $t = 4.000780 \times 10^4$ s, $t = 6.000884 \times 10^4$ s, $t = 8.000754 \times 10^4$ s, and $t = 1.000028 \times 10^5$ s, respectively. Note that we omit the planet from these snapshots.

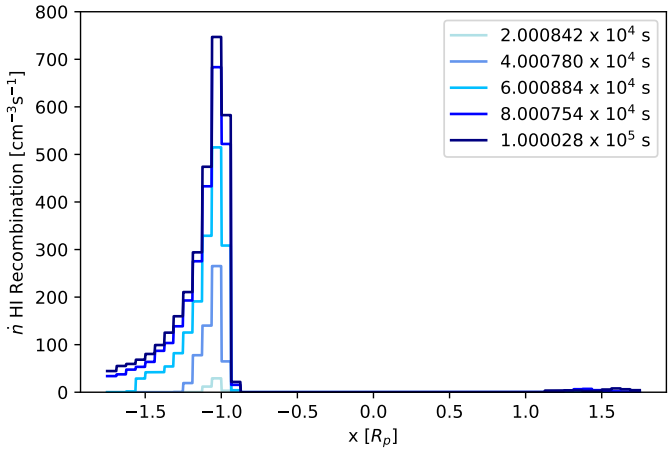

Figure 5.3: The rate of recombining hydrogen atoms along the x direction for the first handful of time steps in the simulation denoted in the legend.

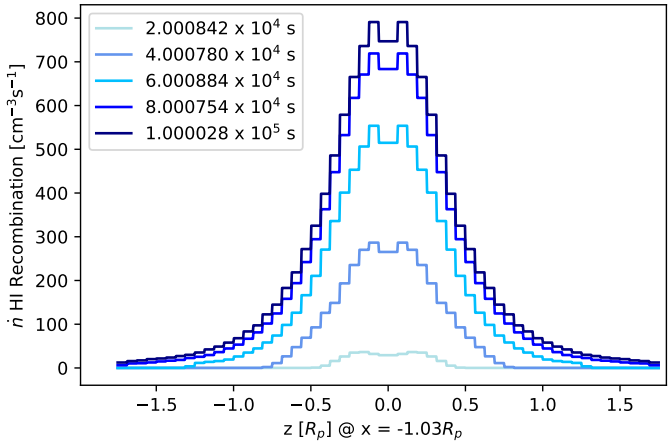

Figure 5.4: The rate of recombining hydrogen atoms along the z direction at the peak of recombination in the x direction (i.e $x = -1.03R_p$) for the first handful of time steps in the simulation denoted in the legend.

of the way through the simulation in Figure 5.5, showing the planet and the rate of hydrogen atoms recombining with electrons. The host star is to the left in the negative x-direction. Notice that the rate of recombination looks very similar to the bottom snapshot in Figure 5.2. We show $\dot{n}$ on the y axis as a function of the x-direction and as a function of the z direction at the peak of recombination in the x direction at $x = -1.03R_p$ in Figure 5.6. This recombination begins over $0.5R_p$ away from the planet, similar to the recombination rate that occurred 4.000080×10^5 seconds earlier, and peaks at $x = -1.03R_p$ with $\dot{n} = 743.01$ cm^{-3} s^{-1}. We note that this $\dot{n}$ value is not exactly the same as the value at 5% of the simulation, but is very close.

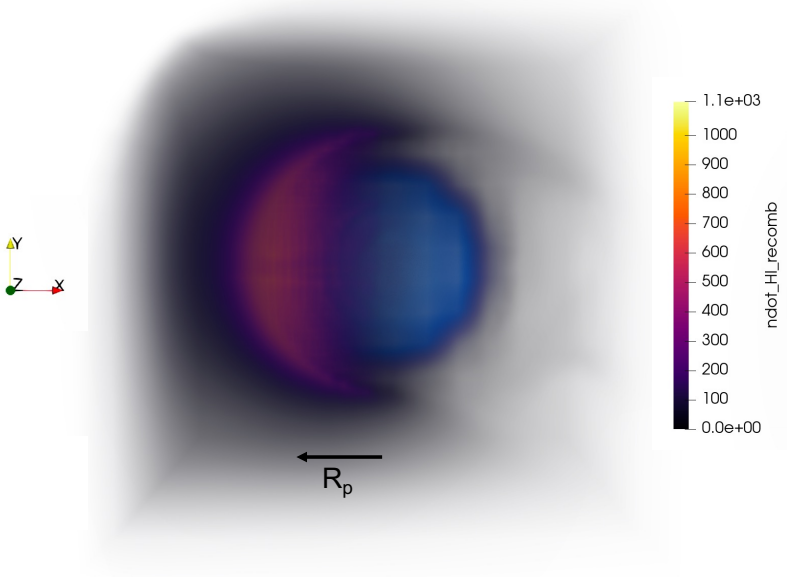

Figure 5.5: A snapshot at $t = 5.000108 \times 10^5$ s showing the planet (blue) and the rate of ionized hydrogen recombining with electrons in the atmosphere in units of cm^{-3} s^{-1} (purple) with the radius of the planet denoted for scale. The host star is to the left of the planet.

50% of the way through the simulation at $t = 1.000002 \times 10^6$ s, the peak rate of recombination remains around the same value. This lack of change is consistent

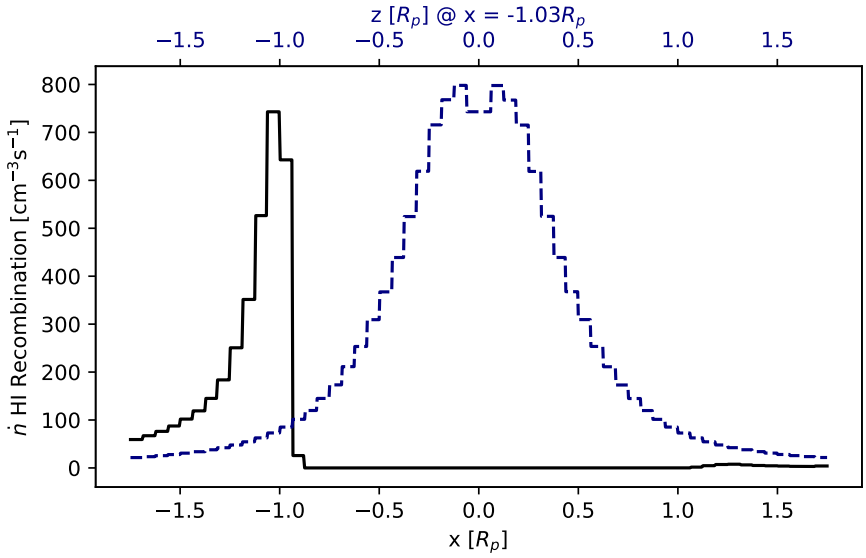

Figure 5.6: The black curve is the rate of recombination along the x direction of the simulation, while the dashed blue curve is the rate of recombination along the z direction at the peak of combination in the x direction (i.e., $x = 1.0293R_p$) at $t = 5.0000108 \times 10^5$ s.

even through the end of the simulation at $t = 2.000001 \times 10^6$ s. We conclude that the simulation reached a quasi-static state at 5% of the simulation, or $t = 1.000028 \times 10^5$ s, with little variability in the peak rate of recombining hydrogen atoms. Nonetheless, the asymmetry of the atmosphere shown throughout remains a significant result. We find that the presence of a stellar wind can indeed impact the structure of a close-in gas giant planet's atmosphere. Although we did not see evidence of an asymmetric atmosphere for HAT-P-18b, we also could not rule it out completely. Applying the exact parameters of HAT-P-18b in `Athena Æ` could demonstrate similar results as the ones we present here, which would provide reason to observe multiple transits of HAT-P-18b in hopes of detecting an asymmetric extended atmosphere.

We may have been able to find evidence for more variability if we also modeled

levels 3 and 4, which are additional layers of the planet's atmosphere. Because Wesleyan's HPCC is limited to a physical core count of 24, we could only simulate the first three levels for this run. To obtain more complete results, we could run an additional simulation on the cluster that is limited to modeling the remaining levels. Then, we could merge the results into a complete, successful run. This process would take a much longer period of time than if we had access to a cluster that could handle a higher CPU core count, thus enabling us to run the simulation in its entirety with every level included in one single go. Although it would be more computationally expensive to run this simulation in parts on Wesleyan's HPCC, it is worth noting. One major takeaway from our work is that the HPCC is a powerful resource for future efforts of 3D modeling here at Wesleyan.

Chapter 6

Conclusion

In this thesis, we present our observations of two transits of the close-in gas giant HAT-P-18b using an ultra-narrow band filter centered on the He I 1083 nm line installed on the 200" Hale Telescope at Palomar Observatory. We detected $0.46 \pm 0.12\%$ excess helium absorption in the upper atmosphere of the planet. We converted this signal to estimate an atmospheric mass loss rate between $8.3^{+2.8}_{-1.9} \times 10^{-5}$ and $2.62^{+0.46}_{-0.64} \times 10^{-3}$ M_J Gyr^{-1}. We then modeled the escaping atmosphere of a generic hot Jupiter using the 3D code, `Athena Æ`, and briefly analyzed our results in context with our target. Although our simulation results were not complete, we were still able to present an asymmetric quasi-static atmosphere for a generic close-in gas giant exposed to ionized radiation from its host star. We find that we require a bigger cluster, capable of a higher physical CPU core count, or additional computation time, so we can model every layer of the atmosphere of a planet and potentially simulate further variability throughout the run.

6.1 Future Work

6.1.1 Future Helium Targets

Our detection presents the faintest system with detected helium absorption thus far. For reference, the next faintest system with detected helium outflow is

WASP-107b with a J magnitude of 9.4. Of the 11 planets identified in Kirk et al. (2020) as promising targets for potential helium escaping atmospheres, a majority of them are challenging targets with $J > 10.5$. Our photometric approach opens the door for observing planets around such faint stars to build upon the small population of planets with measured metastable helium absorption in their upper atmospheres. Future studies of He I extended atmospheres will enable better calibrated mass loss models used to uncover the mechanisms of the long-term evolution of the general close-in exoplanet population.

6.1.2 The Effect of Planetary Magnetic Fields on Outflows

As mentioned in Sections 4.3 & 4.4, the difference in helium outflow signatures in the handful of planets with confirmed excess helium absorption in their atmospheres is of particular interest to us. More specifically, we are interested in how individual planetary magnetic fields can affect the outflow signatures of close-in gas giant planets by either shepherding its gas or interacting with its host star's own magnetic field. Cauley et al. (2015) present a method to estimate the strength of a planetary magnetic field with extended atmosphere observations, where they model pre-transit signal for HD 189733b, a hot Jupiter, as resulting from a bow shock. Bow shocks occur when a host star's stellar wind interacts with the magnetic field of its planet. From their bow shock model, the authors were able to provide a lower limit of the strength of HD189733b's magnetic field of 28 G using physical parameters derived from their bow shock model, such as the mass density of the stellar wind, the relative velocity of the planet and the wind, and the thermal pressure of the wind. Nortmann et al. (2018) measured an asymmetric He I transit for WASP-69b, which can potentially be a target of

interest for determining the magnetic field strength for planets with helium outflows. Repeated follow-up observations of planets with confirmed helium extended atmospheres may lead to our ability to estimate their magnetic field strengths, enabling us to reach a better understanding of the role of magnetic fields in the atmospheric escape of He I gas.

6.1.3 Modeling HAT-P-18b

An additional method to understand the structure of the metastable helium population in the upper atmospheres of close-in gas giants is modeling them. Each exoplanetary helium detection is of necessity to improve current atmospheric mass loss models, such as the ones presented here by Oklopčić & Hirata (2018) and McCann et al. (2019). Using `Athena Æ` to model our target system, HAT-P-18b, may allow us to predict the asymmetry and variability of its planetary atmosphere depending on its host star. But in order to produce fruitful results, we require a larger cluster that is capable of running all established domains within `Athena Æ` or an additional period of time to run the simulation in parts, and a better understanding of the star's stellar wind strength. If we had unlimited computation time, we could model the atmosphere of a hot gas giant throughout its migration history. We could run multiple simulations where we maintain all of the same planet and host star parameters, except for the semi-major axis. This work could demonstrate exactly when in a hot Jupiter's lifetime does it reach a separation where it begins to experience significant atmospheric mass loss. Additionally, future work on `Athena Æ` could extend the hydrogen atmosphere modeling to instead simulating the He I 1083 nm gas in a planet's atmosphere. This would require a much more in depth understanding of the 3D MHD code and the physics

behind it, and the time and resources to run many test runs, but would be the first of its kind.

Our understanding of atmospheric mass loss is essential for revealing the exact mechanisms that affect the evolution of the general close-in planet population. Our ability to observe the He I 1083 nm line from both ground- and space-based facilities to determine present-day atmospheric mass loss for close-in gas giants establishes the present as the ideal time to study the varying atmospheres of these planets. Future helium outflow detections will directly contribute to the calibration of current mass loss models that can demonstrate the long-term evolution of close-in exoplanets.

Bibliography

Allart, R., et al. 2019, A&A, 623, A58

—. 2018, Science, 362, 1384

Alonso-Floriano, F. J., et al. 2019, A&A, 629, A110

Anderson, D. R., et al. 2017, A&A, 604, A110

Berger, M. J., & Colella, P. 1989, Journal of Computational Physics, 82, 64

Bernath, P. F., & Colin, R. 2009, Journal of Molecular Spectroscopy, 257, 20

Bonomo, A. S., et al. 2017, A&A, 602, A107

Bourrier, V., Lecavelier des Etangs, A., & Vidal-Madjar, A. 2015, A&A, 573, A11

Bradley, L., et al. 2020, astropy/photutils: 1.0.0

Cauley, P. W., Kuckein, C., Redfield, S., Shkolnik, E. L., Denker, C., Llama, J., & Verma, M. 2018, AJ, 156, 189

Cauley, P. W., Redfield, S., Jensen, A. G., & Barman, T. 2016, AJ, 152, 20

Cauley, P. W., Redfield, S., Jensen, A. G., Barman, T., Endl, M., & Cochran, W. D. 2015, ApJ, 810, 13

Cauley, P. W., Shkolnik, E. L., Ilyin, I., Strassmeier, K. G., Redfield, S., & Jensen, A. 2019, AJ, 157, 69

Colella, P. 1990, Journal of Computational Physics, 87, 171

Colón, K. D., & Ford, E. B. 2011, PASP, 123, 1391

Cutri, R. M., et al. 2003, VizieR Online Data Catalog, II/246

Esposito, M., et al. 2014, A&A, 564, L13

Foreman-Mackey, D., et al. 2021, exoplanet-dev/exoplanet v0.4.4

France, K., et al. 2016, ApJ, 820, 89

Fulton, B. J., et al. 2017, AJ, 154, 109

Gelman, A., & Rubin, D. B. 1992, Statistical Science, 7, 457

Hartman, J. D., et al. 2011, ApJ, 726, 52

Hoffman, M. D., & Gelman, A. 2011, The No-U-Turn Sampler: Adaptively Setting Path Lengths in Hamiltonian Monte Carlo

Jakosky, B. M., Slipski, M., Benna, M., Mahaffy, P., Elrod, M., Yelle, R., Stone, S., & Alsaeed, N. 2017, Science, 355, 1408

Jensen, A. G., Redfield, S., Endl, M., Cochran, W. D., Koesterke, L., & Barman, T. 2012, ApJ, 751, 86

Kipping, D. M. 2013, MNRAS, 435, 2152

Kirk, J., Alam, M. K., López-Morales, M., & Zeng, L. 2020, AJ, 159, 115

Kirk, J., Wheatley, P. J., Louden, T., Doyle, A. P., Skillen, I., McCormac, J., Irwin, P. G. J., & Karjalainen, R. 2017, MNRAS, 468, 3907

Lightkurve Collaboration et al. 2018, Lightkurve: Kepler and TESS time series analysis in Python, Astrophysics Source Code Library

Loyd, R. O. P., et al. 2016, ApJ, 824, 102

Mamajek, E. E., & Hillenbrand, L. A. 2008, ApJ, 687, 1264

Mansfield, M., et al. 2018, ApJL, 868, L34

Martins, J. H. C., et al. 2015, A&A, 576, A134

Mayor, M., & Queloz, D. 1995, Nature, 378, 355

Mayor, M., et al. 2009, A&A, 493, 639

McCann, J., Murray-Clay, R. A., Kratter, K., & Krumholz, M. R. 2019, ApJ, 873, 89

Murray-Clay, R. A., Chiang, E. I., & Murray, N. 2009, ApJ, 693, 23

Ninan, J. P., et al. 2020, ApJ, 894, 97

Nortmann, L., et al. 2018, Science, 362, 1388

Oklopčić, A. 2019, ApJ, 881, 133

Oklopčić, A., & Hirata, C. M. 2018, ApJL, 855, L11

Owen, J. E. 2019, Annual Review of Earth and Planetary Sciences, 47, 67

Owen, J. E., & Jackson, A. P. 2012, MNRAS, 425, 2931

Owen, J. E., & Wu, Y. 2017, ApJ, 847, 29

Parker, E. N. 1958, ApJ, 128, 677

Piaulet, C., et al. 2021, AJ, 161, 70

Piskorz, D., Knutson, H. A., Ngo, H., Muirhead, P. S., Batygin, K., Crepp, J. R., Hinkley, S., & Morton, T. D. 2015, ApJ, 814, 148

Ricker, G. R., et al. 2014, in Society of Photo-Optical Instrumentation Engineers (SPIE) Conference Series, Vol. 9143, Space Telescopes and Instrumentation 2014: Optical, Infrared, and Millimeter Wave, ed. J. Oschmann, Jacobus M., M. Clampin, G. G. Fazio, & H. A. MacEwen, 914320

Saltzman, J. 1994, Journal of Computational Physics, 115, 153

Salz, M., et al. 2018, A&A, 620, A97

Seager, S., & Sasselov, D. D. 2000, ApJ, 537, 916

Seeliger, M., et al. 2015, MNRAS, 451, 4060

Spake, J. J., et al. 2018, Nature, 557, 68

Stassun, K. G., Collins, K. A., & Gaudi, B. S. 2017, AJ, 153, 136

Stefansson, G., et al. 2017, ApJ, 848, 9

Stone, J. M., Gardiner, T. A., Teuben, P., Hawley, J. F., & Simon, J. B. 2008, ApJS, 178, 137

Struve, O. 1952, The Observatory, 72, 199

Tian, F. 2015, Annual Review of Earth and Planetary Sciences, 43, 459

Tian, F., Chassefière, E., Leblanc, F., & Brain, D. 2013, Atmospheric Escape and Climate Evolution of Terrestrial Planets, ed. S. J. Mackwell, A. A. Simon-Miller, J. W. Harder, & M. A. Bullock, 567

Vidal-Madjar, A., et al. 2004, ApJL, 604, L69

Vidal-Madjar, A., Lecavelier des Etangs, A., Désert, J. M., Ballester, G. E., Ferlet, R., Hébrard, G., & Mayor, M. 2003, Nature, 422, 143

Vidotto, A. A., & Cleary, A. 2020, MNRAS, 494, 2417

Virtanen, P., et al. 2020, Nature Methods, 17, 261

Vissapragada, S., et al. 2020, AJ, 159, 278

Walker, G. 1995, Nature, 378, 332

Wallack, N. L., et al. 2019, AJ, 158, 217

Wilson, J. C., et al. 2003, in Society of Photo-Optical Instrumentation Engineers (SPIE) Conference Series, Vol. 4841, Instrument Design and Performance for Optical/Infrared Ground-based Telescopes, ed. M. Iye & A. F. M. Moorwood, 451–458

Winn, J. N. 2010, Exoplanet Transits and Occultations, ed. S. Seager, 55–77

Winn, J. N. 2014, Transits and Occultations

Wolszczan, A., & Frail, D. A. 1992, Nature, 355, 145

Yelle, R. V. 2004, Icarus, 170, 167

Youngblood, A., et al. 2016, ApJ, 824, 101